

# Synthesis of magnetic nanoreactors for the removal of heavy metals from wastewater and drinking water

Álvaro Martín Gallo Córdova

Máster en Ingeniería Química



MÁSTERES  
DE LA UAM  
2018 - 2019

Facultad de Ciencias



**MASTER UNIVERSITARIO EN INGENIERÍA QUÍMICA**

**Curso académico 2018-19**

**Trabajo Fin de Master**

**SYNTHESIS OF MAGNETIC NANOREACTORS FOR THE  
REMOVAL OF HEAVY METALS FROM WASTEWATER AND  
DRINKING WATER**

**Autor: Álvaro Martin Gallo Córdova**

**Directores: María del Puerto Morales Herrero, PhD**

**Eva Mazarío Masip, PhD**

**Tutor: Pilar Herrasti González, PhD**

# Contents

1. Abstract.....	1
2. Objectives .....	2
3. Introduction.....	3
3.1. Wastewater problematic.....	3
3.2. Water treatment.....	4
3.3. Iron oxide magnetic nanoparticles .....	4
3.3.1. Characteristics.....	5
3.3.2. Application.....	6
3.4. Lead in drinking water and wastewater.....	8
4. Materials and methods .....	9
4.1. Chemical reagents .....	9
4.2. Nanoreactors preparation method .....	9
4.2.1. Iron precursor preparation.....	10
4.2.2. Iron oxide magnetic nanoparticles synthesis .....	10
4.2.3. Silica-shell coating.....	11
4.2.4. Mesoporous silica-shell coated nanocomposites .....	11
4.3. Adsorption experimentation.....	12
4.3.1. Adsorption kinetics .....	13
4.3.2. Adsorption isotherms.....	14
4.4. Characterization technics .....	15
4.4.1. X-ray diffraction .....	15
4.4.2. Fourier-transform infrared (FTIR) spectroscopy .....	15
4.4.3. Thermal gravimetric analysis and differential scanning calorimetry .....	16
4.4.4. Vibrating sample magnetometry (VSM) .....	16
4.4.5. Transmission electron microscopy .....	17
4.4.6. N <sub>2</sub> adsorption isotherms at 77 K.....	17

4.4.7.	Inductively coupled plasma optical emission spectroscopy .....	17
5.	Results and discussion .....	18
5.1.	Magnetic nanoreactors synthesis.....	18
5.1.1.	Characterization .....	18
5.1.2.	Effect of porogenic agent.....	22
5.2.	Lead removal.....	26
5.2.1.	Effect of the pH.....	26
5.1.1.	Effect of the adsorption time.....	27
5.1.2.	Equilibrium isotherm modelling .....	29
5.1.	Future work .....	32
6.	Conclusion .....	33
7.	Bibliography .....	34
8.	Annexes.....	39

## 1. Abstract

---

Due to the incessant environmental deterioration and the possible affectations in human health, four different 50 nm magnetic nanoreactors (NRs) were design and prepared. These complex materials stand as a wastewater treatment sustainable alternative for heavy metals removal due their ability to confine large quantities of residues in smaller volumes and being able to be separated from the aqueous media by magnetic harvesting. The NRs were prepared by coating a 13 nm magnetite core with a silica-shell doped with two different porogenic agent. The nanoreactors underwent a thermal treatment to remove the porogenic agent and increase their surface area for the heavy metal removal process. It was possible to demonstrate that the coating and calcination were performed correctly by means of FTIR TGA, TEM, DSC and VSM. The organic content was indeed eliminated allowing the formation of the mesoporous silica-shell without altering the magnetic properties of the core.

Adsorption experiments were performed with the nanoreactors by using different lead solutions. The pH effect was analyzed together with lead speciation diagram and a value of 5.5 was selected as optimum due the adsorption capacity obtained and to prevent the precipitation of lead as  $\text{Pb}(\text{OH})_2$  at pH values higher than 6. The effect of contact time was analyzed by varying the experimentation time from 5 minutes to 24 hours. The obtained results were adjusted to pseudo-first order, pseudo-second order and Elovich kinetic models. The data was best fitted to pseudo-second order showing that the rate-limiting step is the surface adsorption. The optimum contact time were the equilibrium adsorption capacity is reached was of 2 h. The effect of the initial concentration was also studied and the results were adjusted to three isotherm models: Langmuir, Freundlich and Temkin. The experimental data best fitted the Langmuir model. Therefore, it can be assumed that the adsorption takes place in monolayer. The maximum adsorption capacity values for NR-1, 2, 3 and 4 were of 32, 35, 34 and 35 mg of lead/g of NRs respectively. Theoric calculations indicated that lead ions were not able to diffuse through the nanoreactor pores and they seem to be adsorbed only at the external surface. This means that external forces may be needed to take advantage of the nanoreactor full capacity.

## 2. Objectives

---

The main objective of this research is to develop a high performance material for wastewater and drinking water treatment, specifically for the removal of heavy metals present in this type of water. This material must have certain characteristics that will make it a better treatment route compared to materials commonly used in this type of process. For this reason, and due to the results previously obtained in the research group of the Department of Materials for Health and Environment of the Institute of Materials Science of Madrid (ICMM), nanoreactors with mesoporous surface and magnetic core will be developed and compared. For this, different syntheses will be carried out in which variables, such as the type and amount of porogenic agent in the functionalization of iron oxide magnetic nanoparticles will be evaluated. On the other hand, in the batch experimentation for heavy metal removal, the pH of the media, the effect of heavy metals initial concentration and the effect of time will be analyzed. Based on all of this, the following specific objectives are proposed:

- To obtain the nanoreactors magnetic core by the thermal decomposition method for the synthesis of magnetic iron oxide nanoparticles (MNPs)
- To functionalize the MNPs with tetraethyl orthosilicate (TEOS) and porogenic agent (PA) to form the SiO<sub>2</sub> shell onto the magnetic core.
- To determine the optimal molar ratio (TEOS:PA) in the nanoreactors synthesis.
- To compare different types of porogenic agents (C16TMS and C18TMS) by analyzing their influence in the achievement of a greater surface area and a better performance in the removal of heavy metals.
- To allow the rising of NRs mesopores via thermal treatment by eliminating the porogenic agent doped in the nanocomposites silica-shell preserving the magnetic properties of the core.
- To establish the optimum conditions for the removal of heavy metals.
- To analyze the equilibrium adsorption isotherms and kinetic models that will explain the sorption process.

## 3. Introduction

---

### 3.1. Wastewater problematic

With the increasing of global population in future decades the challenge of providing clean water for communities will be greater by 2050. It can be observed, that because the depletion of water sources and contamination of water, in many fast-growing cities the challenges in developing water resources or infrastructure are increasing in order to meet populations needs [1]. The growing industrialization and urbanization has incited the population growth, resulting in the increase of wastewater into the environment. Because of this, many developed countries have decided to strengthen their environmental policies and minimize the water pollution by regulating industrial activity regarding the discharge of heavy metals as wastewater into the environment [2].

As mentioned, the excessive release of heavy metals into water has become a worldwide problematic concerning the environment and human health due the incessant deterioration of water quality [3]. These heavy metals are considered persistent-contaminants and unlike organic contaminants, they cannot be easily degrade into harmless products [4]. The principal sources of heavy metals are the chemical-intensive industries where Pb, As, Cd, Cu, Cr, Ni and Zn are the most hazardous and can be discharged into the environment as industrial wastewater [5]. The main sources of these contaminants are the following industries: metal surface treatment, metal coating, batteries industry, petroleum refineries, textile industry. mining among others [4].

The continuous heavy metal discharge into the environment has been affecting not only the environment, but the human health. Most of heavy metals can be assimilated and stored into the human body which could be the main cause of several diseases [6]. It has been proven that heavy metal intoxications could affect directly to the central nervous functions, cardiovascular system and many other organs such as kidneys and liver. These toxic effects are long lasting due their difficult degradation even at low concentrations [7]. Therefore, it is of great significance to eliminate and remove these contaminants from aqueous effluents and to avoid its discharge as industrial wastewater [6].

### **3.2. Water treatment**

During the last decades, several methods for drinking water and wastewater treatment have been studied. It is important to establish, that even though there are many different technics for the removal of heavy metals, the ideal treatment should be the one that could meet the maximum contaminant level standards established by the governmental entities, and the national and international organizations [5]. Therefore, many treatment techniques have been developed and compared. Chemical precipitation, oxidation/reduction, membrane filtration, ion-exchange and adsorption are some of the most common treatments for the removal of inorganic contaminants [8, 9].

For the selection of a specific treatment technique it is necessary to evaluate the economic impact and the level of heavy metals initial concentrations. In a common wastewater treatment process, the removal of heavy metals take place throughout the chemical and physical treatments [10]. Nowadays it has been recognized that adsorption is a very effective and affordable technic for heavy metal removal. There have been numerous studies with different adsorbents onto several kinds of heavy metals [11, 12, 13]. The selection of the adsorbent is crucial when maximizing efficiency in the removal process. It is very important that the material used as adsorbent presents high adsorption capacities and allows a non-complex separation from the aqueous media [10]. In this sense, magnetic materials offer an advantage of the easy separation by means of a magnet. Moreover, magnetic interactions between particles can be minimized by reducing the particle size to the nanometer range, giving rise to a superparamagnetic behaviour. Therefore, there is a great deal of attention in solid-phase extraction based on magnetic nanoparticles: materials with high surface area, good stability in a wide pH range, capable of being very selective, and easy to recover and re-use [14].

### **3.3. Iron oxide magnetic nanoparticles**

Nanotechnology can be applied in the resolution or improvement of problems related to water quality, being the use of nanoparticles a trending alternative. Iron oxides are common compounds, which are well-known to be present in the environment and can be easily synthesized in the laboratory via different studied methods as small iron oxide nanoparticles. During the last decades there have been a great interest in the development and optimization of MNPs synthesis techniques due their widely application areas [15].

### 3.3.1. Characteristics

It could be considered as a nanoparticle an inorganic or organic material with diameters ranging from 1 to 100 nm, which have many novel properties as their size can influence in many processes [16]. On the other hand, what makes magnetic MNPs of great interest is that they present unique characteristics, such as their magnetic properties, easily functionalization, high surface area to volume ratio, fast kinetics, strong adsorption capacities, high reactivity, which are useful in a broad range of disciplines including wastewater treatment [17].

The magnetic behavior of MNPs is due to the strong magnetic moment of the iron atom induced by the four unpaired electrons in its  $3d$  orbitals. As it is shown in Figure 3. 1, when iron atoms are arranged as crystals, different magnetic states can be displayed.

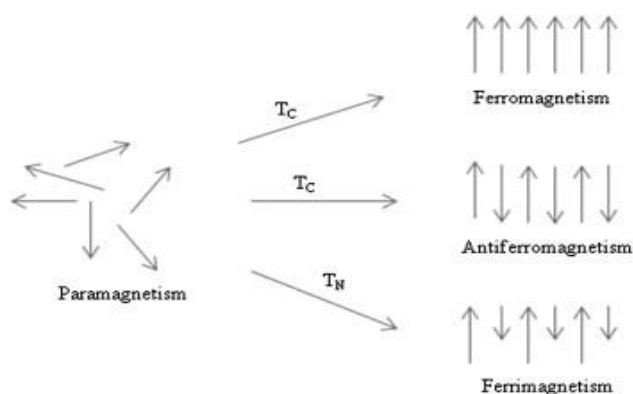


**Figure 3. 1** Alignment of individual atomic magnetic moments in different types of material [18].

When the individual atomic moments are randomly organized it can be classified as a paramagnetic state, where the crystal has a zero net magnetic moment, unless it is subjected to an external magnetic field. On the other hand, in a ferromagnetic state all the magnetic moments are aligned without an external field. In the case of a ferrimagnetic crystal, there exist two moments of different magnitude leading to a net magnetic moment. But, if they were of the same strength, the crystal will hold no net magnetic moment, arising an antiferromagnetic state [18].

The nanoparticles used in this work are formed by a core of iron oxide, mainly magnetite ( $\text{Fe}_3\text{O}_4$ ) or maghemite ( $\gamma\text{-Fe}_2\text{O}_3$ ). Maghemite contains only  $\text{Fe}^{3+}$  ions, half of them coordinated tetrahedrally and the other half octahedrally. On the contrary, in the case of magnetite there are present  $\text{Fe}^{2+}$  and  $\text{Fe}^{3+}$  ions in a molar ratio of 1:2,  $\text{Fe}^{2+}$  ions are all coordinated octahedrally

while half of the  $\text{Fe}^{3+}$  ions are in tetrahedral holes and the other half in octahedral holes. Both materials present an inverse spinel crystal structure, leading to a ferromagnetic behaviour [19].

In the case of small iron oxide nanoparticles its reduction in size (<15 nm) produces a change in the material magnetic behavior where it goes from a ferrimagnetic state to a superparamagnetic state in which the magnetic moment in each particle fluctuates of direction, obtaining a zero net magnetic moment at room temperature [20]. This means that in absence of magnetic field, particles behave as a paramagnet but when the magnetic field is applied, their magnetic moment is  $10^4$  larger than for a paramagnetic material, allowing its movement control with a magnet.

### 3.3.2. Application

Magnetic nanoparticles cover a wide range of applications in the industrial sector, where they can be used as magnetic seals in motors, magnetic recording media, among other things. It is important to acknowledge that for every magnetic nanoparticles application it is necessary that the material present specific properties. An example of this could be its usage in data storage, where the particles need to have a stable and switchable magnetic state to represent bits of information, and that this state is not affected by changes of temperature [20].

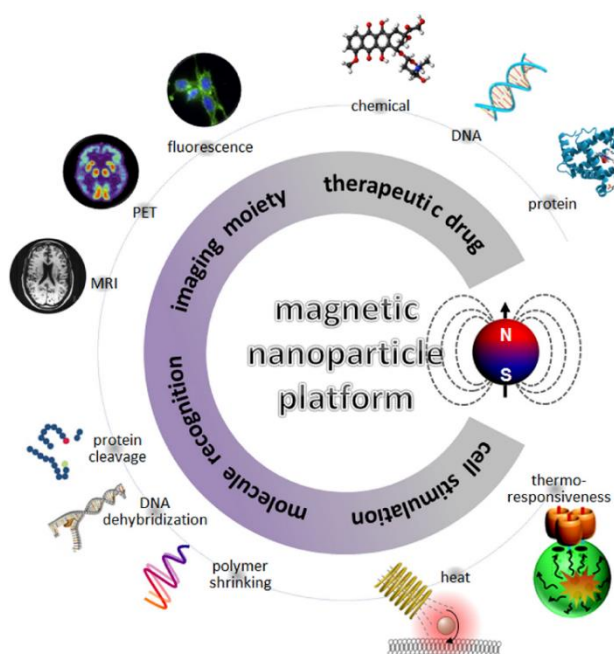


**Figure 3. 2** Schematic representation of biomedical and biotechnological applications of MNPs [21].

Iron oxide magnetic nanoparticles can be used in different disciplines and applications including magnetic recording media, and catalyst [18]. The most common using, as it is shown in Figure 3. 2, is in biomedical and biotechnological applications due their biocompatibility compared to other magnetic materials [22]. They have been widely used as contrast agents for magnetic resonance imaging and therapy agents as targeted drug delivery vehicles for cancer treatment [23, 24, 25, 26]. It is important to state that for *in vivo* applications the particles must be coated with a biocompatible polymer so large aggregates, changes of structure and biodegradation could be prevented [24].

On the other side, magnetic carrier methods are commonly used in several processes such as separation of biological cells, coal desulphurization and wastewater treatment [27]. Iron oxide magnetic nanoparticles can be used as sorbents for heavy metal removal from water, as they are easy to synthesize at low cost. Because their magnetic capacity, they can be easily removed by magnetic harvesting after the sorption process, being this an advantage versus other materials [14].

In the present work, a synthesized magnetite magnetic nanoparticles were functionalized and underwent a thermal treatment to develop a complex material with enough surface area to be a high performance sorbent for heavy metals removal process. As this kind of complex materials could provide a confined space where a reaction could be hosted, many studies have cataloged them as nanoreactors (NRs) for catalytic reactions capable of increasing the reaction efficiency due to their high catalytic activity [28]. In sorption processes its name is due the surface reaction were the adsorbate attaches to the surface of the adsorbent [29].

NRs are considered as a kind of nanostructured material with a wide range of applications areas and fields such as chemical storage, contaminant removal, compartmentation and drug loading. The advantage of this type of complex material is that the nanoreactor can provide a void space between the magnetic core and the shell which will increase sorption and chemical reaction [30]. Mesoporous silica is an approachable way for the achieving of high performance nanoreactors. Silica is an appropriate matrix because its tunable pore size can lead to high surface area and large pore volumes, in addition of being biocompatible and biodegradable [31]. Finally, these NRs made of inorganic compounds are expected to be quite robust and last for longer times once they are prepared in comparison to organic based nanocomposites (chelators).

### **3.4. Lead in drinking water and wastewater**

In the present work, the prepared NRs adsorption capacity was tested by using lead in the heavy metal removal experiments as it is one of the most hazardous and common metals in drinking water and industrial wastewater. Exposure to this kind of compound may cause development of autoimmunity where the immune system attacks its own cells provoking: kidneys diseases, circulatory and nervous system failures, among other diseases [5]. In addition, it has been demonstrated that lead is one of the most threatening contaminants because even at extremely low concentrations can cause brain damage in children [32].

Most of lead contamination comes from corrosion of household plumbing and natural erosion [33, 34]. Within industrial contamination, the principal source of lead discharge onto water are the chemical industry, mining industry and metallurgy [35]. Nevertheless, there exist regulations of national and international entities that consider the lead permissible levels in drinking water and wastewater. The World Health Organization (WHO) has set the quality standard for acceptable levels of lead in drinking water to 10 ppb, which is the value adopted by the European Union since 2013, and by Royal Decree-Law in Spain since 2014 [36, 37]. Also, according to the Royal Decree-Law 60/2011 in Spain the permissible lead discharge levels into wastewater is 7.2 ppb after a 0.45  $\mu\text{m}$  membrane filtration [38].

## 4. Materials and methods

### 4.1. Chemical reagents

The chemical reagents used for the synthesis of the nanoreactors and the adsorption tests are shown in Table 4. 1 where it is detailed each of the names, purity, cost and supplier. It can be observed that the most expensive chemical reagent is the C18TMS, used as porogenic agent in the NRs preparation.

**Table 4. 1** Summary of the chemical reagents used for the nanoreactors synthesis.

Compound	Acronim	Purity (%)	Supplier	Cost
Ethanol	EtOH	96	Panreac AppliChem	18 €/L
Cyclohexane	C <sub>6</sub> H <sub>12</sub>	≥ 99	Sigma-Aldrich	84 €/L
Octadecene	C <sub>18</sub> H <sub>36</sub>	90	Sigma-Aldrich	44 €/L
Iron chloride hexahydrate	FeCl <sub>3</sub> .6H <sub>2</sub> O	≥ 98	Sigma-Aldrich	47 €/kg
Ammonium hydroxide	NH <sub>4</sub> OH	28-30	Sigma-Aldrich	33 €/L
Tetraethyl orthosilicate	TEOS	≥ 99	Sigma-Aldrich	69 €/L
Polyoxyethylene(5)nonylphenyl ether	IGEPAL CO-520	-	Sigma-Aldrich	480 €/kg
Hexadecyltrimethoxysilane	C16TMS	99	Sigma-Aldrich	230 €/L
Octadecyltrimethoxysilane	C18TMS	99	Sigma-Aldrich	4840 €/L
Lead chloride	PbCl <sub>2</sub>	98	Sigma-Aldrich	111 €/kg

### 4.2. Nanoreactors preparation method

The NRs preparation followed the scheme presented in Figure 4. 1, where the synthesized MNPs were coated in two steps with a silica-shell doped with different porogenic agents, and then calcined at 400 °C for the micro and mesopores formation and the increase of the surface area.

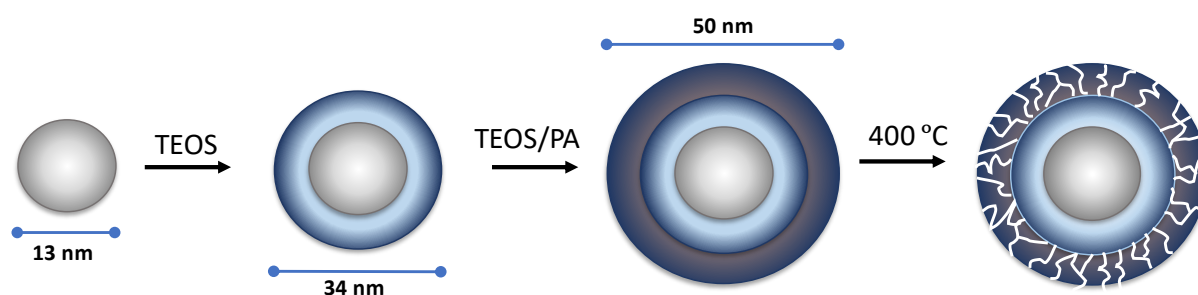


**Figure 4. 1** Schematic representation of nanoreactors preparation.

#### 4.2.1. Iron precursor preparation

For the synthesis method used to prepare the MNPs, it is necessary to consider an iron precursor that allows the reaction and particles formation [39]. In this work, an iron oleate precursor was prepared by mixing, in a two-necked round-bottom flask, 10.8 g of  $\text{FeCl}_3 \cdot 6\text{H}_2\text{O}$  with 45 g of sodium oleate in 60 mL of distilled water, 80 mL of ethanol and 140 mL of hexane. One of the flask necks was sealed with a glass cap and in the other neck a cooling system was placed. The flask was then located into an oil bath and magnetically mixed at 70 °C until a reflux started, and then the reaction was left for 4 hours. Once the mixture was cooled the cooling system was turned off and the mixture was transferred to a separation funnel so the aqueous phase could be separated and discarded. This last step was repeated for 3 times after adding distilled water. The obtained solution was placed in a rotary evaporator (Buchi Rotavapor R-100) at 60 °C and 90 rpm for 1 hour. Once hexane and ethanol were evaporated, the final product was left in an inox-oven at 50 °C during night.

#### 4.2.2. Iron oxide magnetic nanoparticles synthesis

Thermal decomposition method was performed to synthesize monodisperse iron oxide nanoparticles using iron oleate as precursor in an organic media. For this, 4.5 g of liquid iron oleate was weighted with 1.4 g of oleic acid. Then, with the help of 50 mL of octadecene, the mixture was transferred to a 250 mL three-necked round-bottom flask. As shown in Figure 4. 2, the flask was placed in a heating mantle where a nitrogen continuous flux, mixing mechanical aid, temperature indicator and a cooling system were located and sealed to allow a nitrogen environment and a good temperature control.

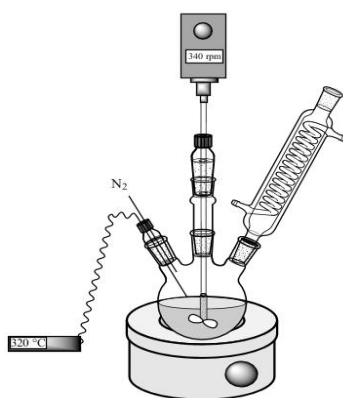


**Figure 4. 2** Experimental set-up for nanoparticles synthesis.

The mixing was settled to 340 rpm until 65 °C were reached, and the nitrogen flux was turned off at 100 °C. Afterwards, the heating mantle was turned off one hour after octadecene boiling point was reached (320 °C). The sample was collected and washed several times with ethanol and centrifuged at 8000 rpm for 15 minutes until organic precursors and reactants were removed. The washed sample was suspended in cyclohexane for further functionalization.

#### **4.2.3. Silica-shell coating**

In this work  $\text{SiO}_2@\text{Fe}_3\text{O}_4$  nanoparticles were used as platform for deriving other nanoparticle architectures. In order to fixate the MNPs into a  $\text{SiO}_2$  shell, the monodispersed nanoparticles obtained, underwent a scale up microemulsion process using Igepal CO-520 as surfactant to achieve a micellar-sol-gel-combined coating route [40]. Thus, 83 mg of NPs were mechanically mixed using a shaker for 30 minutes with a mixture, previously prepared by sonication, of 300 mL of cyclohexane and 13.3 mL of polyoxyethylene(5)nonylphenyl ether (0.56 mmol, Igepal CO-520, containing 50 mol % hydrophilic group). Afterwards, 2.16 mL of  $\text{NH}_4\text{OH}$  30 % were added into the mixture and shaken for 15 minutes to form a transparent, brown solution of reverse microemulsion. Subsequently, 2.5 mL of tetraethyl orthosilicate (TEOS) was added dropwise and shaken for 24 hours. After the reaction time was completed, the mixture was washed 3 times with methanol, which causes the NPs precipitation, and another 3 times with ethanol. After each wash, the NPs were collected by centrifugation at 8000 rpm for 15 minutes.

#### **4.2.4. Mesoporous silica-shell coated nanocomposites**

In order to prepare a mesoporous silica-coated nanocomposite (NRs), the obtained  $\text{SiO}_2@\text{Fe}_3\text{O}_4$  were coated with a mixture of TEOS and a porogenic agent (PA), that was varied between two kinds: hexadecyltrimethoxysilane (C16TMS) and octadecyltrimethoxysilane (C18TMS), which molecule structures are shown in Figure 4. 3. From this process it is possible to achieve high preparations yields. By using only 10 mg of MNPS the amount of NRs obtained was 10 times greater.

Also, the molar ratio of TEOS:PA was varied to compare the influence of the amount of porogenic agent in the NRs surface area and silica-shell thickness.

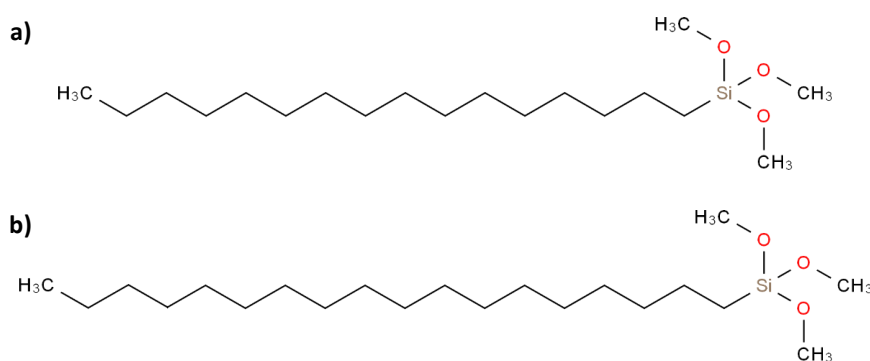


**Figure 4. 3** a) Hexadecyltrimethoxysilane (C16TMS) and b) Octadecyltrimethoxysilane (C18TMS) molecule structures.

The nanoreactors were prepared by stirring TEOS and PA (at a molar ratio of 2.6:1 and 4.7:1, for each experiment and each type of PA) in a mixture of 10 mL of distilled water, 132 mL of ethanol and 6 mL of aqueous 30 % NH<sub>4</sub>OH solution with SiO<sub>2</sub>@Fe<sub>3</sub>O<sub>4</sub> nanoparticles at room temperature for 5 minutes. Afterwards, the volume of TEOS and PA was added according to Table 4. 2, and shaken for 7 hours. The product was collected by centrifugation at 8000 rpm for 15 minutes, washed 3 times with ethanol, and calcined at 400 °C in air for 3 hours to remove the porogenic agent and to allow the mesopore formation in the surface of nanoreactors.

**Table 4. 2** Tetraethyl orthosilicate and porogenic agent quantities for nanoreactors preparation.

Sample	Porogenic agent	Volume (μL)	Molar ratio (TEOS:PA)
NR-1	C16TMS	110:40	4.7:1
NR-2	C18TMS	110:40	4.7:1
NR-3	C16TMS	90:60	2.6:1
NR-4	C18TMS	90:60	2.6:1

### 4.3. Adsorption experimentation

The batch lead adsorption experiments were carried out at room temperature (20 °C) in a plastic 15 mL vial containing 5 mg of NR and 10 mL of lead solutions with different initial concentrations. The mixture was then shaken during different times and the NR was collected by magnetic separation. Figure 4. 4 summarizes how the experimentation was performed.

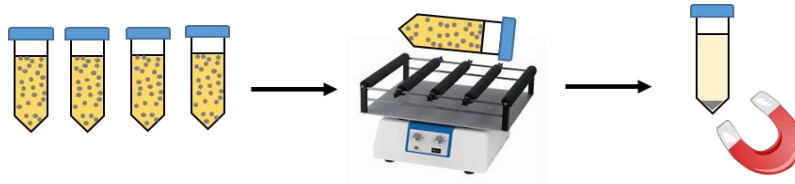


**Figure 4. 4** Schematic representation of the experimental set up for batch adsorption experiments.

The pH value of lead solutions is considered a very important parameter concerning adsorption experimentation. pH analyses were carried out for values from 3 to 7 with an adsorption time of 180 minutes with a lead initial concentration of 100 mg/L, in the batch experimentation previously explained. The pH values were selected after analyzing the lead speciation diagram because when lead is present in aqueous media it could exist as different species due its protonation degree.

The nanoreactors adsorption capacity at equilibrium was calculated by Equation 4.1 [41].

$$q_e = (C_0 - C_e)V/m \quad \text{Equation 4. 1}$$

Where  $q_e$  is the adsorption capacity equilibrium, in mg of Pb/g of adsorbent;  $C_0$  is the initial concentration of lead, in mg/L;  $C_e$  is the equilibrium concentration of lead, in mg/L;  $m$  is the dry weight of adsorbent, in g; and  $V$  is the volume of lead solution, in L. The percentage of lead removal was obtained by the following equation:

$$\% \text{ Removal} = \frac{(C_0 - C_e)}{C_0} \cdot 100 \quad \text{Equation 4. 2}$$

#### 4.3.1. Adsorption kinetics

In order to understand the mechanism of adsorption and the possible rate – determining step, including mass transport and chemical reaction, kinetics models were analysed. Table 4. 3 summarizes the three different models considered for this work, with its corresponding linearized and non-linearized form of the equations. The rate of change of the adsorption capacity,  $dq_t/dt$ , is settled as function of the adsorption capacity during time,  $q_t$ , and the contact time,  $t$ . The non-linear equations for all three models has been linearized by integration, where the boundary conditions are  $q_t = 0$  in  $t = 0$  and  $q_t = q_t$  in  $t = t$ .

The PFO model is considered valid for long adsorption times in a system near equilibrium. The PSO is known to fit best to most environmental kinetic adsorption processes where the rate-limiting step is the surface adsorption that involves chemisorption, where the removal from a solution is due to physicochemical interactions between two phases [42]. On the other hand,

the Elovich equation neglects desorption and it is known to describe chemisorption well as it is suitable for kinetics far from equilibrium where desorption does not occur due the low surface coverage [43].

**Table 4. 3** Kinetic models equations.

<b>Kinetic model</b>	<b>Equation</b>	<b>Linearized equation</b>	<b>Plot</b>
Pseudo-first order (PFO)	$\frac{dq_t}{dt} = k_1(q_e - q_t)$	$\ln(q_e - q_t) = \ln q_e - k_1 t$	$\ln(q_e - q_t) vs t$
Pseudo-second order (PSO)	$\frac{dq_t}{dt} = k_2(q_e - q_t)^2$	$\frac{t}{q_t} = \frac{1}{q_e^2 k_2} + \frac{t}{q_e}$	$\frac{t}{q_t} vs t$
Elovich	$\frac{dq_t}{dt} = \alpha \exp(-\beta q_t)$	$q_t = \frac{1}{\beta} \ln(\alpha\beta) + \frac{1}{\beta} \ln t$	$q_t vs \ln t$

To obtain the experimental data as function of time, the same batch experimentation was performed in all four nanoreactors at optimum pH and initial lead concentration of 40 mg of Pb/L by varying the adsorption time from 5 minutes to 24 hours.

#### 4.3.2. Adsorption isotherms

In order to understand how an adsorption process is being performed, it is important to describe it and fit it to the best isotherm model. An isotherm is a term used to describe the equilibrium curves in these kind of processes. In the present work, three different isotherm models were considered: Langmuir, Freundlich and Temkin. Table 4. 4 shows the linear and non-linear equations for the models mentioned. In each model, the dependence of the equilibrium adsorption capacity,  $q_e$  (mg of Pb/g of NR) is established as function of the lead equilibrium concentration,  $C_e$  (mg of Pb/L).

**Table 4. 4** Isotherm models equations.

<b>Isotherm</b>	<b>Equation</b>	<b>Linearized equation</b>	<b>Plot</b>
Langmuir	$q_e = \frac{q_m b_0 C_e}{1 + b_0 C_e}$	$\frac{C_e}{q_e} = \frac{1}{b_0 q_m} + \frac{1}{q_m} C_e$	$\frac{C_e}{q_e} vs C_e$
Freundlich	$q_e = K_f C_e^{1/n}$	$\ln q_e = \ln K_f + \frac{1}{n} \ln C_e$	$\ln q_e vs \ln C_e$
Temkin	$q_e = \frac{RT}{b_T} \ln(K_T C_e)$	$q_e = \frac{RT}{b_T} \ln K_T + \frac{RT}{b_T} \ln C_e$	$q_t vs \ln C_e$

The Langmuir adsorption isotherm is the most common model that assumes that the adsorbent surface is homogenous and has a monolayer coverage with a specific number of actives sites

where the molecules of the solute can be adsorbed. Oppositely, Freundlich isotherm model is given for systems with heterogeneous surfaces ( $n$  = heterogeneity factor) where adsorption limited levels does not exist, while the Temkin isotherm model consider that the possible adsorption heat reaction ( $b_t$ , J/mol) of the molecules in the surface layer decreases with the coverage in a linear way [41].

By analyzing the data of final lead concentration and adjusting it to the models mentioned, it is possible to understand the behavior of the process and to obtain the nanoreactors maximum adsorption capacity,  $q_m$  (mg of Pb/g of NR) – (Langmuir Equation). For this experimentation the lead initial concentration was varied from 20 to 100 mg of Pb/L using the same amount of NR (5 mg) at optimum time and pH values.

#### **4.4. Characterization technics**

##### **4.4.1. X-ray diffraction**

The crystal structure of the sample was identified by X-Ray powder diffraction (XRD) performed in a Bruker D8 Advance diffractometer with a graphite monochromator using  $\text{CuK}\alpha$  radiation ( $\lambda = 1.5406 \text{ \AA}$ ). The patterns were collected within  $10^\circ$  and  $90^\circ$  in  $2\theta$ . The XRD spectra was indexed to an Fd-3m space group with cubic structure and the crystal size was calculated by the full width of the half-maximum (FWHM) peak with the greatest intensity (311) by using the Scherrer's equation:  $d_c = k\lambda/\beta \cos \theta$  (Equation 4. 3)

Where  $k$  is the crystallite shape factor (0.89),  $\lambda$  is the wavelength of the X-rays ( $\lambda = 1.5406 \text{ \AA}$ ),  $\theta$  is the Bragg diffraction angle of the (311) plane, and  $\beta$  is the FWHM of the (311) diffraction peak which is the extent between two extreme values of the independent variable located at the highest peak [44].

##### **4.4.2. Fourier-transform infrared (FTIR) spectroscopy**

This is a physical-chemical analytical technique used to categorize the structure of an unidentified composition or a chemical group, and its intensity of the absorption spectra associated with the molecular composition [45]. At temperatures above absolute zero, all the bonds within molecules vibrate. There are numerous kinds of vibrations that cause absorptions in the infrared region, being the easiest to visualize the bending and stretching. If this vibration results in the change of the dipole moment, the molecule will absorb energy at a frequency

which corresponds to the frequency of the bonds natural vibration [46]. To confirm the presence of the silica and porogenic agent coating the FTIR spectra of the samples was obtained by using a Bruker IFS 66VS in the range of 400 – 4000  $\text{cm}^{-1}$ . The samples were prepared by diluting the dried powder in KBr at 2% w/w and fitting them into pellets.

#### **4.4.3. Thermal gravimetric analysis and differential scanning calorimetry**

The thermal gravimetric analysis (TGA) can provide information about different aspects of diverse materials, such as physical phenomena, absorption and desorption, thermal decomposition, among others. It consists in a thermal analysis where the mass of a sample is measured in a range of temperatures changed over time. On the other side, differential scanning calorimetry (DSC) analysis is used to measure the energy absorbed or released when the sample has been heated or cooled, which allows to obtain information about the endothermic and exothermic processes that correspond to the heat adsorption and heat evolution respectively [47].

In order to understand how the nanoparticles functionalization can be modified by temperature (percentage of carbon in the surface), TGA and DSC analysis were performed on the nanoreactors samples using a TA Instruments Q2000 differential scanning calorimeter. Prior to the analysis, samples were dried in an inox-coated oven at 50 °C overnight and the analyses were carried out in a temperature range of 25 to 800 °C at a rate of 10 °C/min in an air environment.

#### **4.4.4. Vibrating sample magnetometry (VSM)**

Magnetic characterization of the samples, were carried out in a vibrating sample magnetometer MagLabVSM, Oxford Instrument with a maximum field of 50 kOe. The sample was dried in an inox-coated oven at 50 °C overnight. Afterwards the samples were accurately weighted and fitted into the sample holder. A hysteresis loop of the powder sample was measured at 290 K up to  $\pm 3$  T. With the resulting data, the values of saturation magnetization ( $M_s$ ) in, magnetic remanence ( $M_R$ ) in emu/g of NR and coercivity ( $H_c$ ) in Oe were obtained for each sample.

Remanence is the ability of the material to retain a certain amount of residual magnetic field when the magnetic force is removed, while magnetic saturation is the maximum value of magnetization where a material does not change upon further increase of the magnetic field. Also the field magnitude necessary to obtain zero magnetization is called coercivity [48].

#### **4.4.5. Transmission electron microscopy**

This technique consists in a beam of electrons that passes through a thin layer of a sample, causing its dispersion in different directions. Depending on the density of the material, some electrons could be dispersed and disappear into the beam. The electrons that have not been dispersed, impact on a screen in the lower part of the microscope, allowing the rise of an "image in the shade" with different luminosity according to the density of the material present in the area of incidence.

Particle size and shape were studied by transmission electron microscopy (TEM) using a JEOL JEM 1010 microscope operated at 100 keV. TEM samples were prepared by placing one drop of a dilute particle suspension on an amorphous carbon-coated copper grid and evaporating the solvent at room temperature. The mean particle size and distributions were evaluated by measuring the largest internal dimension of at least 200 particles. Afterwards, the data were fitted to a lognormal distribution obtaining the mean size ( $\bar{X}$ ) and the standard deviation ( $\sigma$ ).

#### **4.4.6. N<sub>2</sub> adsorption isotherms at 77 K**

This technique was used to analyze the information of the sample porous structure, considering the micro and mesopore. The principal data obtained by this method are the surface area (BET), and the pore sizes and distribution by carrying out the characterization with a TriStar II 320 (Micrometrics) system. The samples were degasified for at least 12 hours at 393 K and 0.1 mbar. Afterwards, the samples were introduced in a liquid nitrogen bath where the nitrogen absorption was measured by its injection in the interior of the samples.

#### **4.4.7. Inductively coupled plasma optical emission spectroscopy**

The iron concentration in the suspensions prior the nanoreactor preparation and the heavy metal determination before and after the adsorption process were carried out on an inductively coupled plasma – optical emission spectrometry apparatus from Perkin Elmer, model OPTIME 2100DV. In the case of the iron determination the wavelengths used were 238.204 and 239.562 nm and for lead determination was 220.353 nm. For the uncoated nanoparticles it is necessary to digest the dispersion prior the analysis in order to have an appropriate determination by eliminating the organic matter that could be present. In this case, an aliquot of the sample (25  $\mu$ L) was diluted in a 1 mL mixture (3:1) of HCl 25 % w/w and HNO<sub>3</sub> 65 % w/w at 90 °C until digestion was obtained (48 h).

## 5. Results and discussion

### 5.1. Magnetic nanoreactors synthesis

In this section, an analysis of the synthesized nanoreactors is presented with the different variables considered and proposed. The materials obtained during the NRs synthesis were characterized by TEM, XRD, FTIR, TGA, ICP-OES. In the case of the  $\text{SiO}_2@\text{Fe}_3\text{O}_4$  and the NRs,  $\text{N}_2$  isotherms for the surface area and pore size analyses were considered too.

#### 5.1.1. Characterization

Iron oxide nanoparticles were synthesized by the decomposition method in organic media, which is commonly used for obtaining monodispersed and crystalline particles. This method is also an approachable way for the synthesis of nanoparticles with tunable sizes and shapes that can be controlled by the reaction time, the temperature, the nature of precursors, the oleic acid content and the nature of solvent and the agitation.

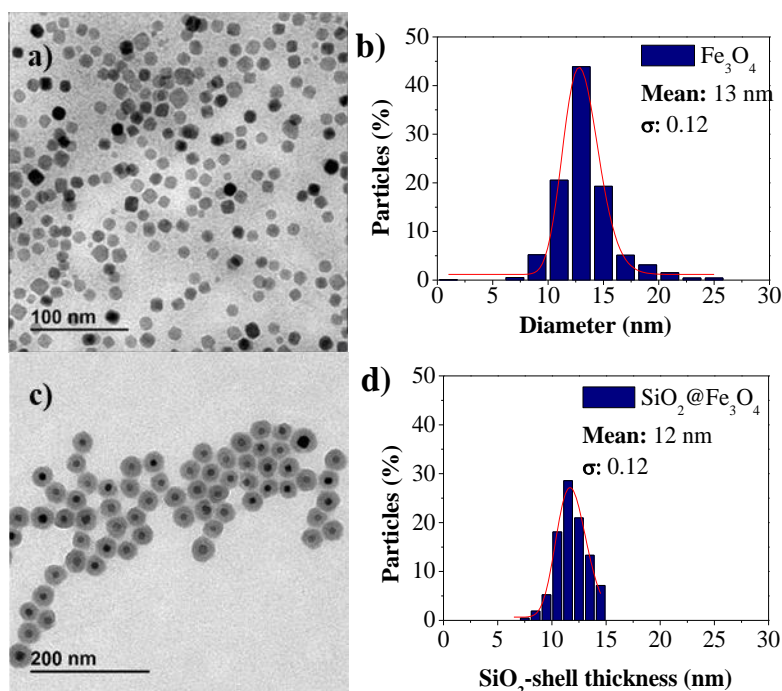


**Figure 5.1** a) TEM image, and b) size distribution of the iron oxide nanoparticles. c) TEM image and d) shell thickness of  $\text{SiO}_2@\text{Fe}_3\text{O}_4$ .

The resulting nanoparticles were characterized by TEM as it is shown in Figure 5.1. The mean particle size and distribution were evaluated and the data was fitted to a lognormal distribution. A mean size of 13 nm and a standard deviation of 0.12 was obtained. Figure 5.2 shows X-ray powder diffraction patterns of the single phase  $\text{Fe}_3\text{O}_4$  synthesized nanoparticles. It can

be observed in the XRD pattern that there are six intense reflections indexed by (220), (311), (400), (422), (511) and (440), which are matched with the spinel structure of the magnetite pattern. Crystal mean size obtained with Scherrer's equation (Equation 4.3 in Section 4.4.1) is 10 nm.

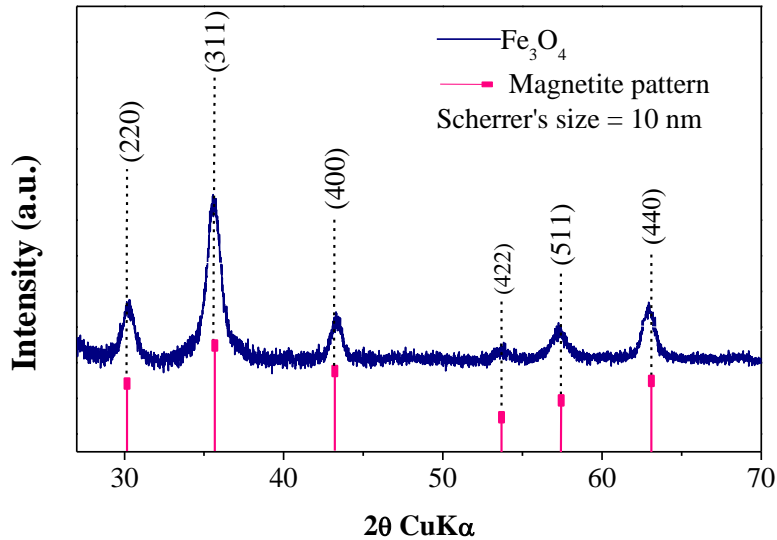


**Figure 5. 2** X-ray diffraction pattern of the synthesized magnetite nanoparticles ( $\text{Fe}_3\text{O}_4$ ).

It is importance to consider that this size value for the MNPs differs from the TEM size because it is only considering the size of the crystallite unit, while the TEM measurements take into account the whole bulk size of the particle. Since one nanoparticle can be constituted by a unique crystallite or more, it is common to obtain a Scherrer's size value lower than the TEM diameter size.

On the other hand, after performing the scale up sol-gel method, a silica-shell coated nanoparticles were obtained. In this process, the shell thickness can be controlled by changing the reaction time or the amount of TEOS in the reaction [49]. As it is shown in Figure 5. 1, TEM images show that the silica was placed uniformly onto de nanoparticles avoiding its agglomeration. It can be seen that most of the nanocomposites have only singles cores. Nanoparticles with no coating were not observed nor pure silica nanoparticles, which means that the amount of TEOS used for the coating was enough or that the silica nanoparticles were removed by centrifugation. Regarding the shell thickness, it can be observed that it is uniform and quite smooth with no distortions. The mean shell thickness was of 12 nm with a standard deviation of 0.12.

The identification of the silica and PA coating and the effect of the calcination in the samples was analysed by FTIR as it is shown in Figure 5. 3. All the spectrums of the NRs, before and after calcination, as well as of the  $\text{SiO}_2@\text{Fe}_3\text{O}_4$ , show an absorption band at approximately  $1080\text{ cm}^{-1}$  which corresponds to the Si-O bond on the nanoparticles surface silica-shell [50]. On the other hand, the spectrums of the pre-calcined NRs (dashed line) show some differences. The small band at  $1475\text{ cm}^{-1}$  is attributed to the C-H absorption, while the bands at  $2931$  and  $2858\text{ cm}^{-1}$  allow the identification of  $-\text{CH}_3$  and  $-\text{CH}_2$  stretch vibrations respectively, because of the presence of hexadecyl and octadecyl groups of the porogenic agents. The band of  $3443\text{ cm}^{-1}$  was ascribed to  $-\text{OH}$  groups on the surface of the particles [51].

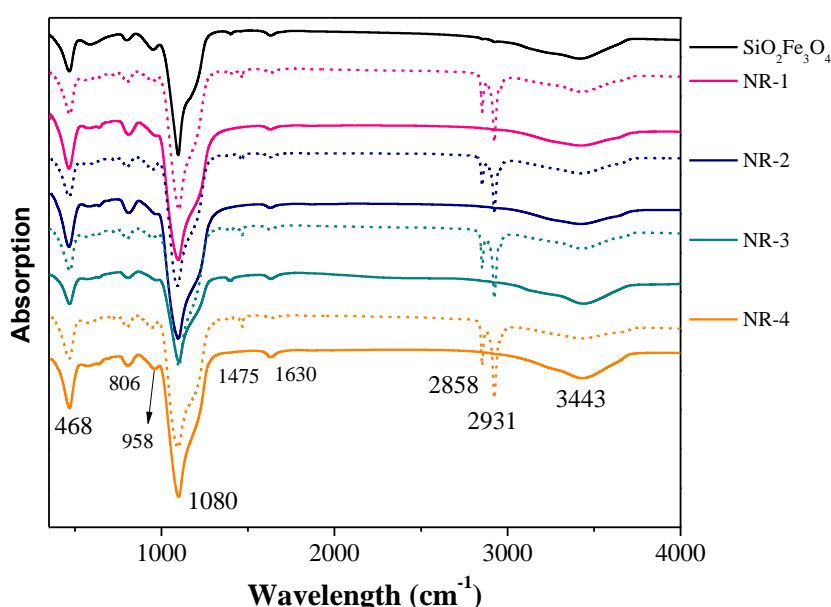


**Figure 5. 3** FTIR spectrum of NRs before (dashed line) and after calcination.

It can be seen from the FTIR results that in the pre-calcined NRs there were absorption bands that correspond to the PAs and the silica-shell, indicating that the coating was successful. Then again, it has been demonstrated that after calcination the carbon from the PA was eliminated and only the mesoporous silica-shell remained.

Figure 5. 4 shows the magnetization curves obtained for each NR at room temperature. Magnetic saturation, remanence and coercivity were obtained from the magnetization loops and the results are shown in Table 5. 1. The remanence obtained values in all NRs were of 0 emu/g of NR, while the values of  $M_S$  were similar for all NRs at 290 K. On the other hand, the NRs showed low coercive fields ( $H_C$ ), being close to the superparamagnetic regime.

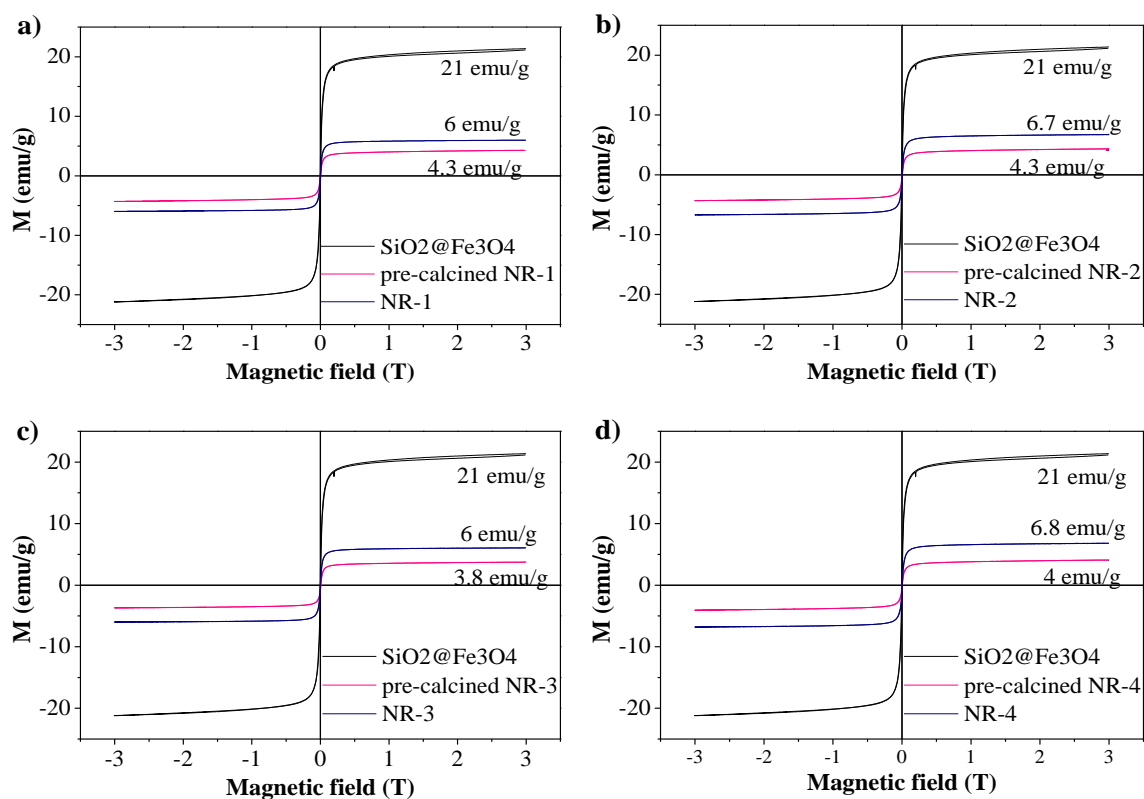


**Figure 5. 4** Magnetization curves for a) NR-1, b) NR-2, c) NR-3, d) NR-4 at 290 K.

The values of magnetic saturation in all cases decrease for the samples previous calcination, which confirms that the particles had undergone a functionalization of silica and the PA (non-magnetic layer that contributes in the weight of the NR).

**Table 5. 1** Magnetic data for the nanoreactors at room temperature.

Sample	$M_S$ (emu/g NR)	$M_R$ (emu/g NR)	$H_C$ (Oe)
SiO <sub>2</sub> @Fe <sub>3</sub> O <sub>4</sub>	21	2	16.4
NR-1	6	0	5.3
NR-2	6.7	0	4.7
NR-3	6	0	27.5
NR-4	6.8	0	7.5

It also can be observed that the NRs (post-calcined) show an increase in the magnetic saturation value up to 6 emu/g of NR due to the removal of the PA molecules with the calcination. The presented value for all NRs is magnetic enough to recuperate the adsorbent from the media by magnetic harvesting after the sorption process. Therefore, the coating process was performed correctly and the silica shell did not interfere with the materials magnetic properties.

### 5.1.2. Effect of porogenic agent

The amount of PA was evaluated by coating  $\text{SiO}_2@Fe_3O_4$  particles with different mixtures of TEOS and PA in order to ensure that the selected amounts previously mentioned are the optimum for NRs preparation. For this comparison, only C16TMS was used and the molar ratio TEOS:C16TMS was varied. The final quantities chosen for NRs preparation are described in Table 4. 2.

As it is necessary to find a better wastewater treatment alternative, an important parameter to consider when preparing this kind of NRs is the cost of the synthesis process. Many other researches of this kind of NRs use C18TMS during its preparation, certainly obtaining good results in the final application [49, 52]. To economize the process previously mentioned one of the limiting parameter to consider is the price of the C18TMS. For this, the characteristics provided in the nanoreactors by C16TMS as porogenic agent are analyzed and compared to the results obtained by using C18TMS.

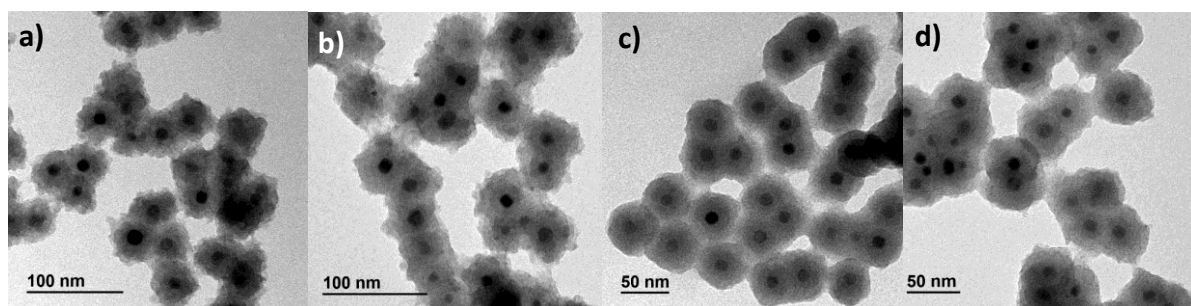


**Figure 5. 5** TEM images of pre-calcined a) NR-1, b) NR-2, c) NR-3, and d) NR-4.

To measure the percentage of PA doped in the silica-shell of the NRs, a thermogravimetric analysis (TGA) was performed onto all the NRs samples. The results obtained from this analysis are shown in Figure 5. 6.

It can be observed the weight loss (%) in the samples after and before calcination. In the case of the samples after calcination, the value obtained was around 4% in all the temperature range for all cases, which means that only water and no organic matter is being eliminated from the samples. On the other hand, the pre-calcined samples show the same 4 % of weight loss in the initial temperature range (from 0 – 250 °C approx.), but all the samples present a significant weight loss until 600-700 °C, which is the doped PA.

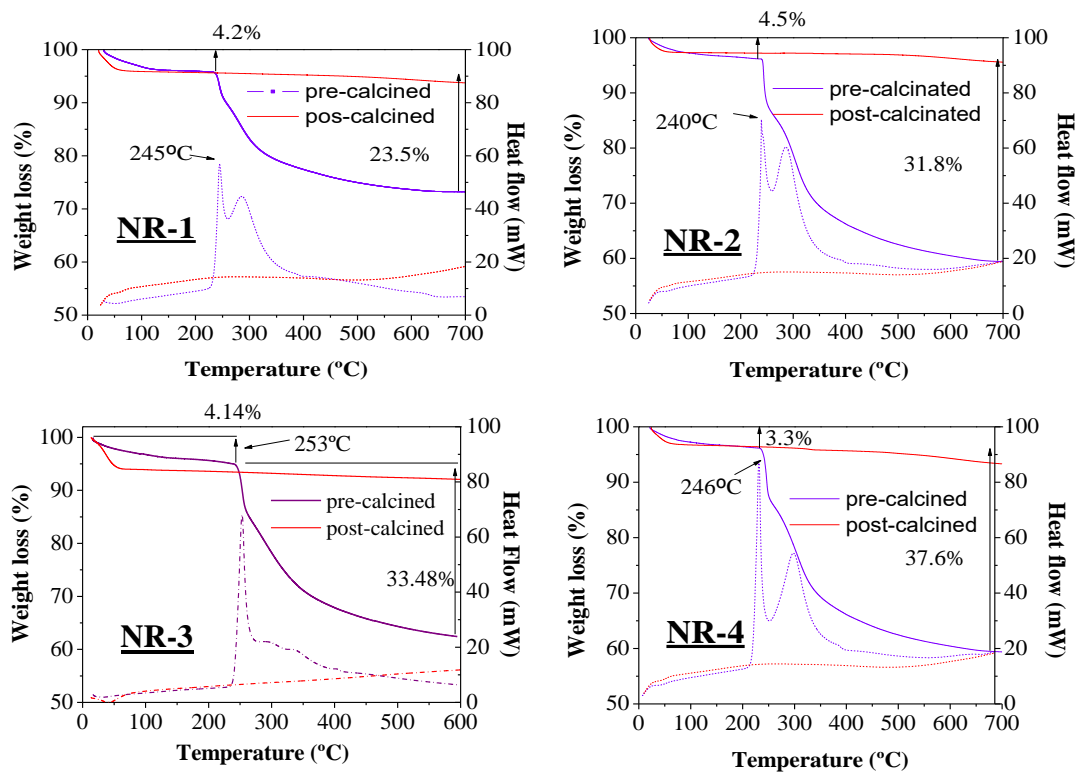


**Figure 5. 6** Thermogravimetric analyses of a) NR-1, b) NR-2, c) NR-3, and d) NR-4.

The obtained results agree with the expected ones and the obtained by FTIR and VSM previously explained. The samples NR-3, and NR-4 presented the highest percentages (33.5 and 37.6 %, respectively) since in their preparation a greater amount of C16TMS (for NR-3) and C18TMS (for NR-4) were used. Also, as it can be seen NR-4 presented a greater value than NR-3, this because C16TMS has a smaller carbon chain than C18TMS. In the case of the samples NR-1 and NR-2 the weight loss is smaller (23.5 and 31.8 %, respectively) due the amount of porogenic agent used, and also the difference by using C18TMS instead of C16TMS, is noticed.

The porosity of NRs was also studied due its influence in the adsorption process. N<sub>2</sub> isotherms were obtained for each sample and the results are shown in Figure 5. 7. This kind of isotherms were described by Brunauer, Emmett and Teller (BET) in 1938 as an extension of the classical Langmuir adsorption isotherm from monolayer to ideal multilayer adsorption and where a limiting case of infinite many layers is considered [53]. The presented isotherms of NRs, pre-calcined NRs, and SiO<sub>2</sub>@Fe<sub>3</sub>O<sub>4</sub> could be described as type II, typically obtained in mesoporous materials, showing at low pressures monolayer and at higher pressures multilayer adsorption [54].

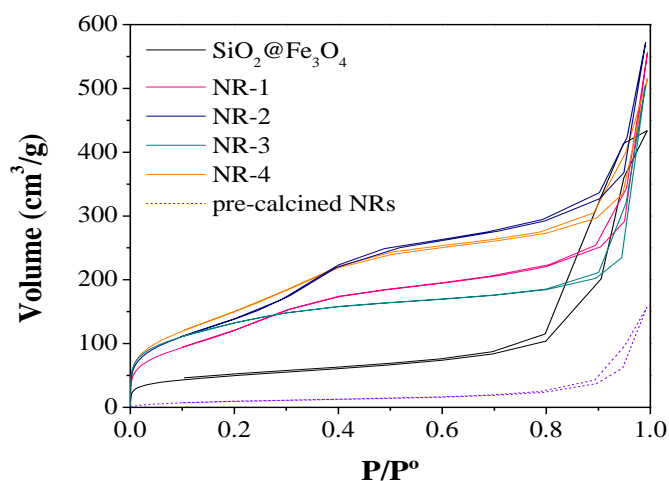


**Figure 5. 7** Nanoreactors N<sub>2</sub> isotherms at 77 K.

Information about the porosity of NRs can be obtained from the N<sub>2</sub> isotherms. All pre-calcined samples showed similar N<sub>2</sub> isotherms and it can be observed that the volume of nitrogen adsorbed is quite low compared to the SiO<sub>2</sub>@Fe<sub>3</sub>O<sub>4</sub> and the NRs which can be addressed to the presence of pores that rises after calcination. Also, the NRs presented a higher porosity than the uncoated SiO<sub>2</sub>@Fe<sub>3</sub>O<sub>4</sub>, and the hysteresis between the adsorption and the desorption branch indicates the existence of mesopores which it is confirmed in Table 5. 2. NR-2 and NR-4, prepared by C18TMS showed a higher volume of nitrogen adsorption than the NRs prepared by C16TMS, agreeing with their surface area values.

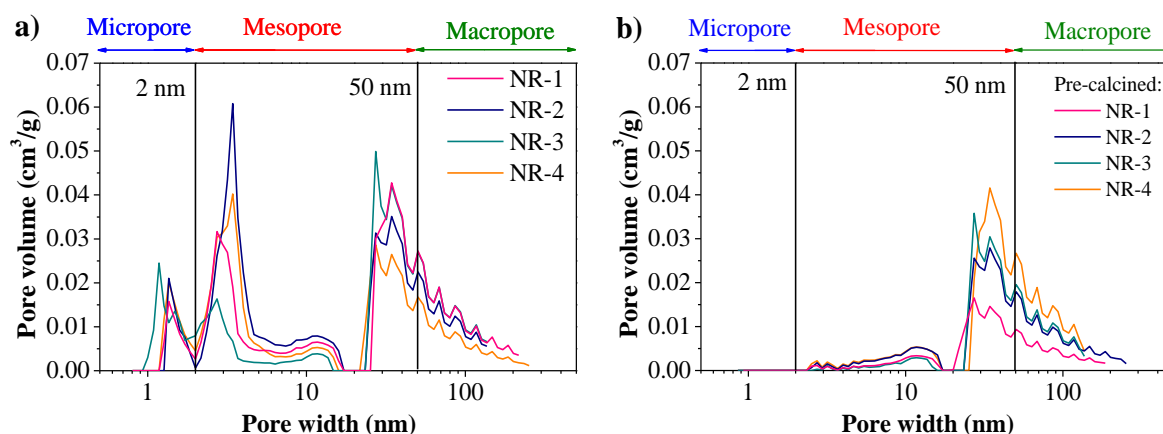


**Figure 5. 8** Nanoreactors pore size distribution. a) after calcination and b) before calcination.

The distribution of pore sizes of NRs were obtained and are shown in Figure 5. 8. As it can be observed all samples presented micropore (less than 2 nm), mesopore (between 2 and 50 nm) and macropore (> 50 nm), being the area obtained for micropores and macropores smaller than the one obtained for the mesopores. On the other hand, the pre-calcined samples presented a quite lower pore volume and no micropore, Table 5. 2. This means that NRs present a higher

volume and adsorption capacity after calcination due the elimination of the PA allowing the formation of mesopores.

**Table 5. 2** Nanoreactors surface area and mesopore volume.

Sample	Porogenic agent	A <sub>BET</sub> (m <sup>2</sup> /g)	V <sub>mesopore</sub> (cm <sup>3</sup> /g)
SiO <sub>2</sub> @Fe <sub>3</sub> O <sub>4</sub>	-	176	0.093
Pre-calcined NR-1	C16TMS	37	0.109
NR-1*	C16TMS	470	0.276
NR-2*	C18TMS	522	0.440
NR-3 <sup>†</sup>	C16TMS	478	0.192
NR-4 <sup>†</sup>	C18TMS	568	0.266

TEOS:PA molar ratio: \*4.7:1 and <sup>†</sup>2.6:1

BET area and pore volume values for each NRs are summarized in Table 5. 2, being the NRs prepared by C18TMS the samples with highest surface area and more mesopore volume, but not that far from the values obtained for NRs prepared by C16TMS. When the amount of organic matter is greater, the more chance of carbon could be coated in the surface of the particles and this will promote the increase of surface are during the calcination. On the other hand, it can be seen that the mesopore volume rises for all NRs which confirms the achievement of the mesoporous silica-shell that will increase the capacity of the material to host the surface reaction. Also, it can be assumed that because the silica-shell already presents mesopores, the values of mesopore volume obtained for the NRs prepared with a greater amount of TEOS its higher than the ones that were prepared with lesser amount.

Table 5. 3 details the cost that implies using one or another PA, as it can be observed the difference between cost per sample is pretty noticeable.

**Table 5. 3** Cost of porogenic agent for each nanoreactor.

Sample	Porogenic agent	Volume (mL/sample)	Cost (€/sample)
NR-1	C16TMS	0.04	0.01
NR-2	C18TMS	0.04	0.19
NR-3	C16TMS	0.06	0.02
NR-4	C18TMS	0.06	0.28

During the characterization of the NRs it was seen that the ones prepared with C18TMS presented better characteristics than the prepared with C16TMS. Nevertheless, the differences

between all NRs were not that distant from each other, which means that NRs with C16TMS could present similar results during its application in adsorption of lead from wastewater.

## 5.2. Lead removal

In order to understand the performance of the sorption process of heavy metals onto the NRs, lead was selected for the batch experimentation. In this section the results of the adsorption equilibrium and kinetics analyses are summarized and discussed.

It is important to understand that this adsorption process is a surface phenomenon where the molecules of  $Pb^{2+}$  are bind to the solid surface of the NRs. In this phenomenon, mass transfer has a great significance were three steps are involved: external diffusion, pore diffusion and surface reaction as it is shown in Figure 5. 9. The first step consists in the transport of the adsorbate ( $Pb^{2+}$ ) from the bulk phase to the external surface of the NR, while the pore diffusion consists in its transport through the NR pores so it can get to the final step were the  $Pb^{2+}$  is attached to the internal surface of the adsorbent, the surface reaction [29].

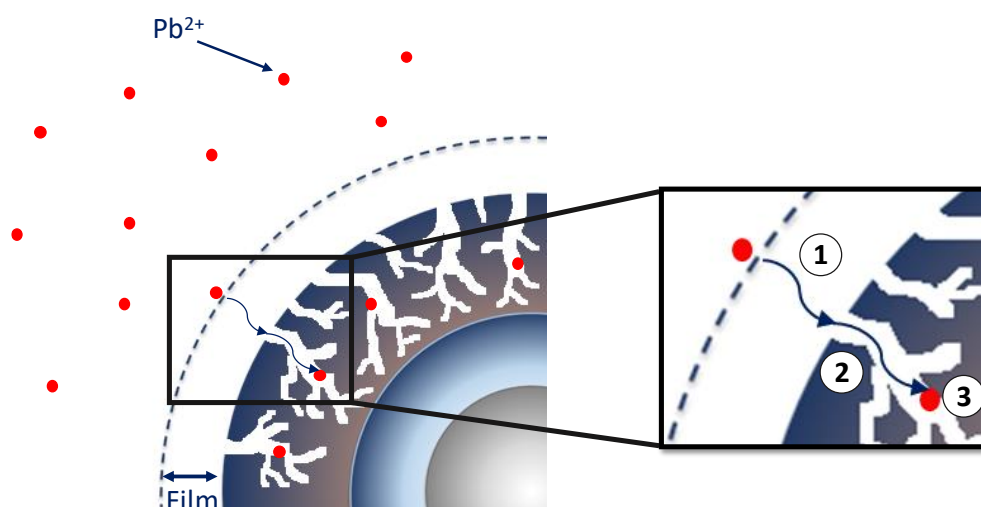


**Figure 5. 9** Schematic representation of  $Pb^{2+}$  sorption process onto the NRs. 1) External diffusion, 2) pore diffusion and 3) surface reaction.

### 5.2.1. Effect of the pH

For the study of the effect of pH, values between 3 and 7 were selected to perform the batch experimentation by using NR-1. It can be seen from Figure 5. 10. a) that after the batch experimentation at different pH values, the obtained  $q_e$  are very similar and the highest adsorption capacity was obtained at a pH of 5 and 7.

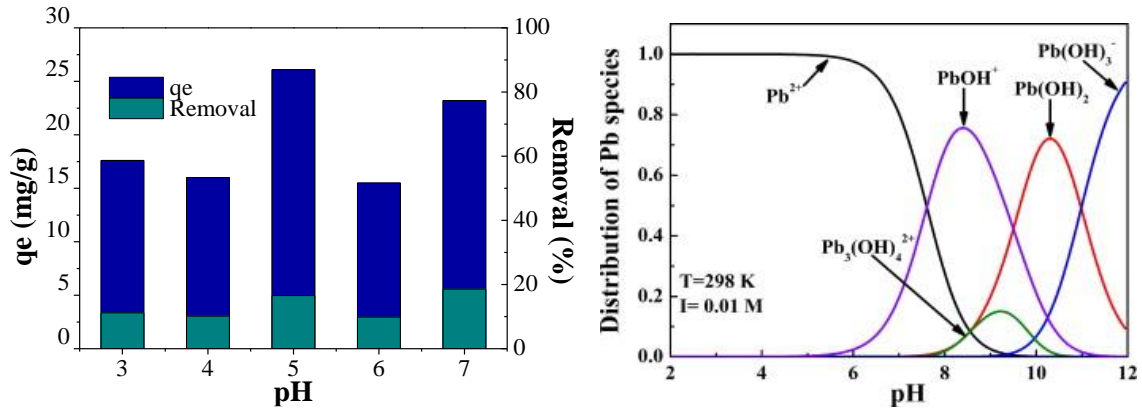


**Figure 5. 10** a) NR-1 adsorption capacity and lead percentage removal for different pH values, and b) speciation diagram of lead as a function of pH extracted from [55].

At different pH values, the lead present in the aqueous media could exist as different species due its protonation degree as it is shown in Figure 5. 10. b). According to lead speciation, at pH values higher than 7, species such as  $\text{Pb}(\text{OH})^+$  and  $\text{Pb}(\text{OH})_2$  are present in the media. Consequently, lead removal can be accomplished by simultaneous precipitation of  $\text{Pb}(\text{OH})_2$  and sorption of  $\text{Pb}(\text{OH})^+$ . This have been proofed with the measurement of the lead initial concentration at different pH values. After varying the pH to 6 and 7 the concentration of Pb of the as prepared solutions decreased with time because the precipitation of lead as  $\text{Pb}(\text{OH})_2$ , while at pH values between 3 and 5.5 remained constant as it can be seen in Table 5. 4. Therefore, to avoid the possibility of lead ion hydrolysis at higher pH, a pH of 5.5 was chosen as optimum.

**Table 5. 4** Pb concentration after and before pH adjustment in the initial concentration solutions ( $C_0$ ).

pH	[Pb] before pH adjustment (mg/L)	[Pb] after pH adjustment (mg/L)
5	79	79
5.5	79	79
6	79	73
7	79	62

### 5.1.1. Effect of the adsorption time

The contact time was studied by performing the batch experimentation at optimum conditions and varying it from 5 minutes to 24 hours. Equilibrium adsorption capacity was calculated for each NR by fitting the experimental data to three kinetic models described in Table 4. 3 with their linearized form. Kinetic parameters are shown in Table 5. 5 and were obtained for pseudo-first order, pseudo-second order and Elovich models.

**Table 5. 5** Kinetic constants of each nanoreactor

Constant	Units	NR-1	NR-2	NR-3	NR-4
Pseudo-first order					
$q_e$	mg/gNR	14.5	14.9	16.2	14.9
$k_1$	-	2E-04	2E-04	2E-04	2E-04
$R^2$	-	0.3	0.3	0.4	0.4
Pseudo-second order					
$q_e$	mg/gNR	23.5	23.4	23.3	23.8
$k_2$	-	0.01	0.01	0.01	9.4E-04
$R^2$	-	1.0	1.0	1.0	1.0
Elovich					
$\beta$	mg/gNR	0.84	0.72	0.64	0.72
$\alpha$	mg/g.min	8.1E+05	6.1E+04	6.4E+03	6.1E+04
$R^2$	-	0.8	0.8	0.8	0.8

Figure 5. 11 shows the obtained results for all NRs, it can be observed that the equilibrium adsorption capacity, calculated by pseudo-second order equation, is similar for all cases. The experimental data best fitted the pseudo-second order model with a determination coefficient ( $R^2$ ) of 1 in the 4 NRs. Because of this, it can be assumed that the rate-limiting step is the surface adsorption and the  $Pb^{2+}$  removal is due to the physicochemical interaction with the NRs [43]. The equilibrium adsorption capacity was reach at 2 h of contact time.

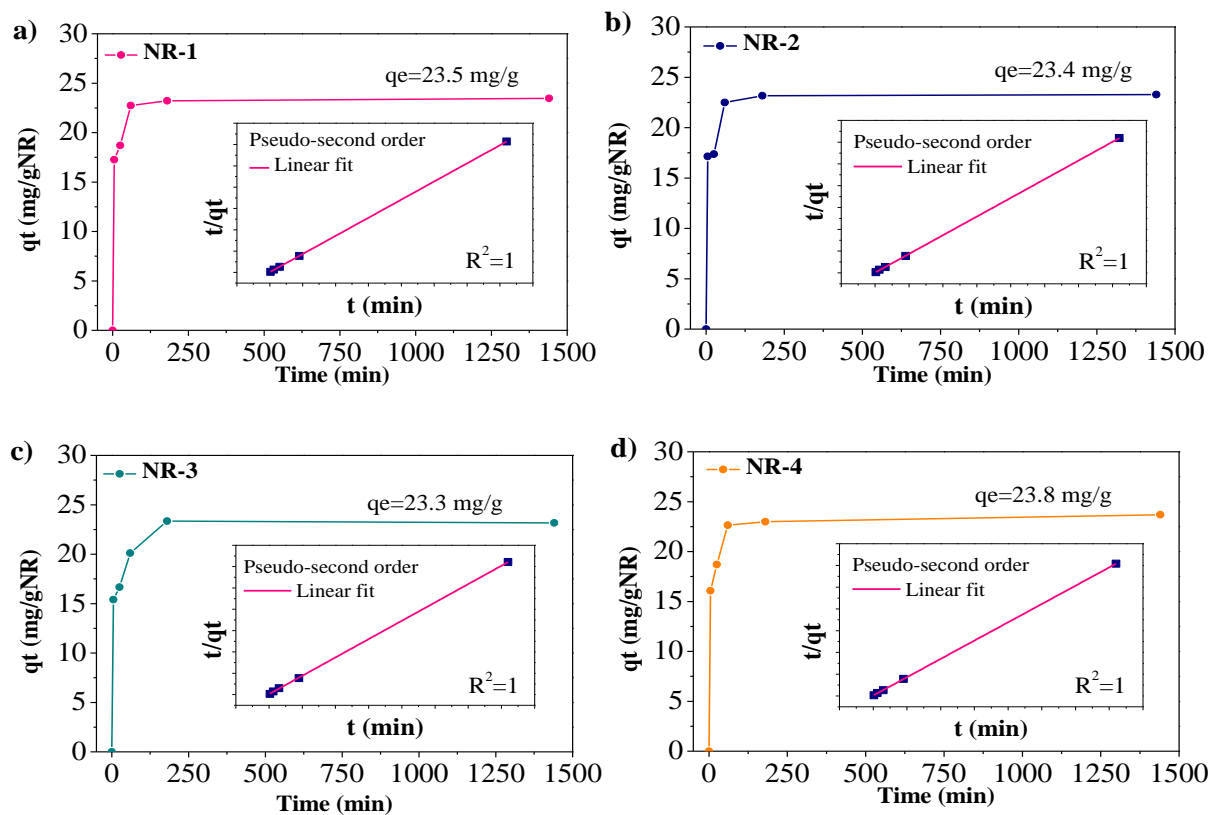


**Figure 5. 11** Effect of contact time on  $Pb^{2+}$  adsorption capacity and linear fit of experimental data for pseudo-first order of a) NR-1, b) NR-2, c) NR-3, and d) NR-4 at room temperature.

### 5.1.2. Equilibrium isotherm modelling

The batch experimentation for the analysis of the effect of lead initial concentration was performed using each NR in a lead solution with different concentrations (20, 40, 60, 80 and 100 mg of Pb/L) at optimum pH (5.5), 3 h of contact time (based on the optimal value obtained from kinetic experimentation) and room temperature. For this analysis, three different isotherm models were considered and fitted to the experimental data obtained. As it is shown in Figure 5. 12, Langmuir, Freundlich and Temkin were considered

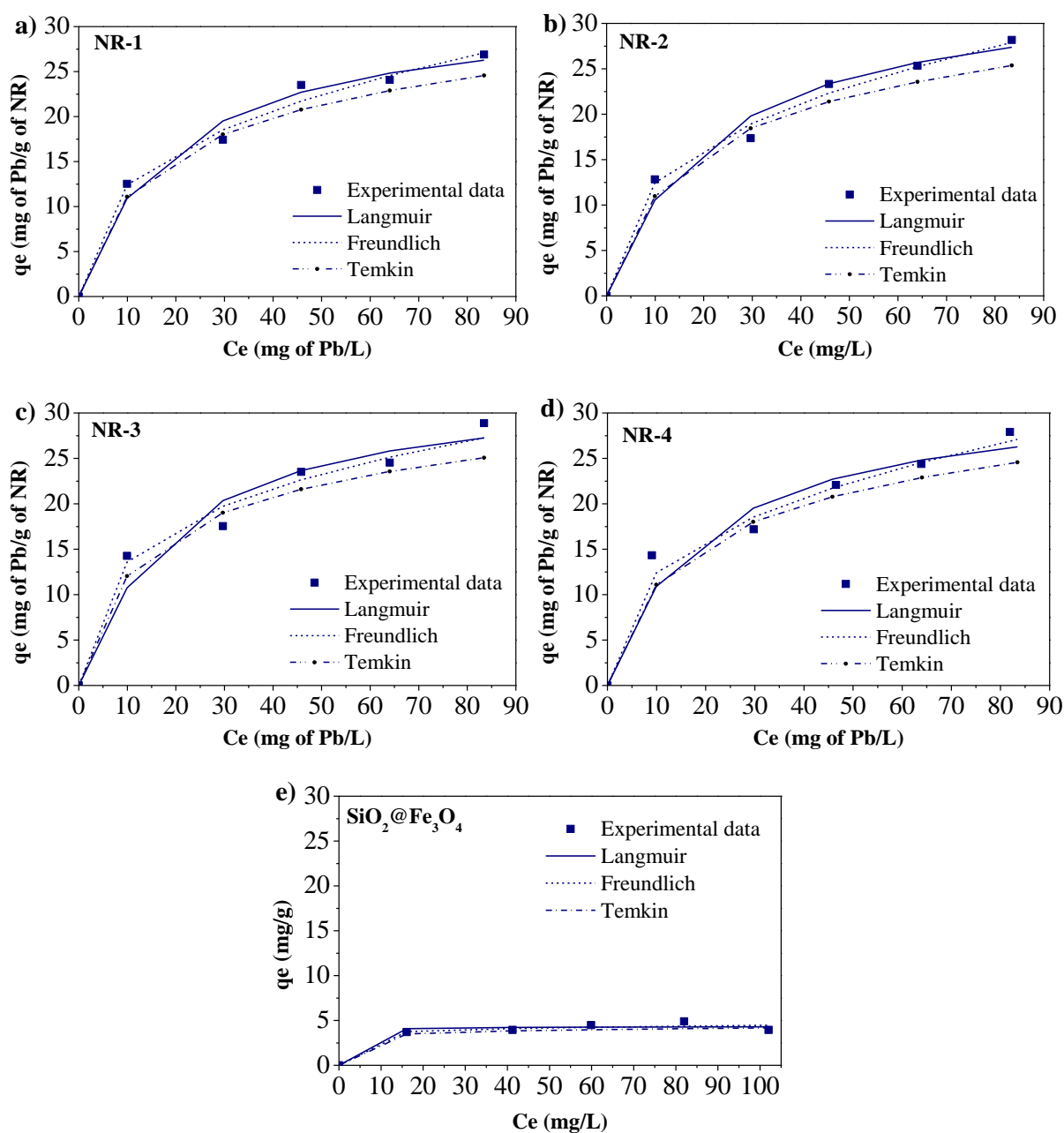


**Figure 5. 12** Adsorption isotherms of a) NR-1, b) NR-2, c) NR-3, and d) NR-4 e) SiO<sub>2</sub>@Fe<sub>3</sub>O<sub>4</sub> (5 mg of NRs, 10 mL of lead solution) at room temperature.

Linearized forms of the isotherms models equations were used as presented in Table 4. 3, considering each of the plots for the linear regressions. Table 5. 6 shows the constants of each model and the determination coefficients ( $R^2$ ) obtained. From this information it can be determined that Langmuir isotherm best describes the experimental data for the sorption process of  $Pb^{2+}$  onto NRs. Therefore, it can be assumed that the adsorption takes place in monolayer and after the maximum adsorption capacity is reached, no further adsorption can be accomplished because no more than one molecule can occupy a specific site.

**Table 5. 6** Calculated isotherms coefficients for each nanoreactor and  $SiO_2@Fe_3O_4$ .

Constant	Units	NR-1	NR-2	NR-3	NR-4	$SiO_2@Fe_3O_4$
Langmuir						
$b_0$	L/mg	0.05	0.04	0.05	0.05	1.10
$q_m$	mg/gNR	32	35	34	35	4
$R^2$	-	0.98	0.97	0.95	0.92	0.97
Freundlich						
$K_f$	$(mg/g)/(L/g)^{1/n}$	5.33	5.25	6.77	7.50	2.88
$1/n$	-	0.367	0.38	0.31	0.29	0.09
$R^2$	-	0.97	0.96	0.93	0.90	0.37
Temkin						
$b_t$	J/mol	357.76	333.12	383.82	404.81	6203.21
$K_t$	L/g	0.58	0.51	0.84	1.02	860.77
$R^2$	-	0.95	0.95	0.89	0.83	0.35

There are many researches of lead adsorption into magnetic nanoparticles that agrees with the obtained results were the sorption process is better described by Langmuir isotherm [56, 57, 58]. All NRs presented similar maximum adsorption capacity ( $q_m$ ) values, and even though the  $q_m$  of each NR is lower than the expected for this kind of complex nanocomposites with high surface area, the obtained results agrees with the characterization of the material and the values of surface area of all NRs. It can be observed that the NRs with greater surface areas, present higher adsorption capacities. Being the NR-4 ( $568\text{ m}^2/\text{g}$ ) the one with the highest  $q_m$  value, 35 mg of Pb/g of NR, while the NR-1 ( $470\text{ m}^2/\text{g}$ ) presents the lowest value, 32 mg of Pb/g of NR. It is important to state that one of the experimental values (20 mg of Pb/L) obtained for the modelling of the adsorption equilibrium isotherms did not adjust quite good as the others values and if it was not take into consideration the maximum adsorption capacity will be greater for all NRs.

The theoretical and ideal estimation of the amount of  $Pb^{2+}$  removed was calculated considering the total surface area and the external surface area. It was assumed that the NRs are perfect spheres were  $Pb^{2+}$  molecules occupy a spherical area on its surface. The experimental data of

the amount  $Pb^{2+}$  removed by 5 mg of NRs was also calculated and the results are shown in Table 5. 7. It can be observed that the amount that could be removed of  $Pb^{2+}$  by the specified amount of NRs is lower than theoretical values, where the total surface area can hold up to 7.62 mg of  $Pb^{2+}$  and the external surface up to 0.6 mg of  $Pb^{2+}$ . The experimental data showed that the highest removed value was of 0.15 mg  $Pb^{2+}$ .

**Table 5. 7** Experimental and theoretical amount of  $Pb^{2+}$  removed by each nanoreactor.

Sample	$m_{exp}$ (mgPb)	$m_{theoric}$ external (mgPb)	$m_{theoric}$ internal (mgPb)	$m_{theoric}$ total (mgPb)	$q_{m\ theoric}$ (mg Pb/g)	External occupancy %	Total occupancy %
NR-1	0.134	0.60	5.71	6.31	1262	22.4	2.1
NR-2	0.141	0.60	6.41	7.01	1401	23.5	2.0
NR-3	0.144	0.60	5.82	6.42	1283	24.1	2.3
NR-4	0.150	0.60	7.02	7.62	1525	24.9	2.0

It can be assumed that lead ions were not able to diffuse through the nanoreactor pores and they seem to be adsorbed only at the external surface, as shown in the theoretical calculations, the external occupancy is greater than the one considering the internal surface (total occupancy). This means that external forces may be needed to take advantage of the nanoreactor full capacity.

On the other hand, adsorption capacity of  $SiO_2@Fe_3O_4$  was also studied and the obtained results are shown in Table 5. 6 and the fitting of the experimental data is shown in Figure 5. 9. It can be seen that the resulting data of  $Pb^{2+}$  adsorption experimentation when using the PA non-doped nanocomposite also fits best to the Langmuir isotherm model, which means that the adsorption occurs in monolayer. However, the obtained value for maximum adsorption capacity was quite smaller compared to the obtained when using NRs. From this it can be concluded, that even though the adsorbate molecules are not diffusing into the NRs pores the adsorption capacity increases after the PA doping, meaning that the NRs surface affinity with  $Pb^{2+}$  increases.

In order to improve the adsorption capacity of NRs it is necessary to consider different parameters. Temperature has an important role in sorption processes because it can improve the diffusion of the adsorbate molecules leading to higher mass transfer from bulk to the boundary layer in the surface of the adsorbent [59]. Many studies have shown that there is an optimal experimentation temperature in which  $Pb^{2+}$  adsorption capacity rises for different adsorbents. This researches had established that the rate of removal is increased with

temperature, but the relationship between the adsorbent and adsorbate is a parameter needed to consider in order to establish the optimal value [60, 61].

Alternatively, another parameter that has a great influence on the sorption process, is the type of agitation used during the batch experimentation. It is necessary to ensure an optimum interaction between the adsorbent and adsorbate so the surface reaction can occur. An adsorptive separation by a porous material can be achieved due the interaction strength influenced by the adsorbent and the properties of the targeted adsorbate molecules. Also, it is important to consider the different diffusing rates because not all components can enter the pores and become rapidly adsorbed [59].

Regarding the use of different PA in the NRs preparation, it was corroborated that the C18TMS NRs presented higher adsorption capacity as they present a greater surface area. Nevertheless, and as mentioned before the  $q_m$  values obtained for each NRs were quite similar between each other, meaning that C16TMS is a comparable PA for this specific process with the optimum parameters used for experimentation. On the other hand, because the adsorbate molecules were not diffusing appropriately due many possible reasons, it is of great importance to analyse such parameters in order to select the best PA.

### **5.1. Future work**

In order to develop more efficient NRs, it would be interesting to analyze other factors that have not been considered in the present work due the lack of time, as it is the adsorption as a function of the solution temperature. Further analyses are also necessary to evaluate the adsorption of co-existing metals (selectivity), desorption and regeneration of the NRs and degradation after adsorption/desorption cycles.

## 6. Conclusion

---

Four different nanoreactors were prepared for the removal of heavy metals present in drinking water and wastewater. These nanoreactors had a magnetite magnetic core of 13 nm which was synthesized by the thermal decomposition method and then functionalized with tetraethyl orthosilicate and two different porogenic agents to allow the formation of the mesoporous shell. The optimal ratio of TEOS and PA was also analyzed and 4.7:1 and 2.6:1 were the values selected for the experimentation. The nanoreactors that were prepared with less amount of TEOS, presented a higher surface area but similar results for lead removal. Also, by using C18TMS as porogenic agent, the nanoreactors presented better results for the surface area than the ones prepared by C16TMS, nevertheless all nanoreactors showed similar results in the sorption experimentation.

The synthesized nanoreactors were characterized by different techniques. TEM analyses showed that the nanoreactors presented a particle size of 50 nm, and the X-ray spectra obtained, showed a Scherrer's size of 10 nm for the magnetic core which also matches with the magnetite pattern. FTIR, TGA and DSC analyses exhibited that the coating and calcination was performed correctly as the carbon was eliminated and only the silica remained. The magnetization results showed that the magnetization of saturation decreases when the particle has a bigger coating, after the calcination the value was greater than before due to the porogenic agent elimination.

Lead was selected for the adsorption batch experimentation which consisted in adding a specific amount of the nanoreactor onto different lead solutions and shaking it for different contact times. The solution pH was analyzed and a value of 5.5 was selected as optimum. The lead speciation diagram was also analyzed, and showed that lead precipitate as  $\text{Pb}(\text{OH})_2$  in pH values higher than 6. The effect of initial concentration was studied for all nanoreactors and the experimental data best fitted Langmuir isotherm model meaning that the adsorption takes place in monolayer. The maximum adsorption capacity for NR-1, 2, 3 and 4 was of 32, 35, 34 and 35 mg of lead/g of NRs respectively. The theoretic calculations showed that NRs were not working at its full capacity due the need of an external force to allow the diffusion through the pores. The nanoreactors with higher surface area presented better results. Kinetics studies showed that the experimental data better fitted pseudo-second order.

Finally, all 4 NRs have similar efficiency under the experimental conditions undertaken and more experiments are needed in order to select the best NR for this process.

## 7. Bibliography

---

- [1] P. Drechsel, M. Qadir and D. Wichelns, *Wastewater: Economic Asset in an Urbanizing World*, Springer, 2015.
- [2] S. Rezania, S. M. Taib, M. F. Md Din, F. A. Dahalan and H. Kamyab, “Comprehensive review on phytotechnology: Heavy metals removal by diverse aquatic plants species from wastewater,” *Journal of Hazardous Materials*, vol. 318, pp. 587-599, 2016.
- [3] H. A. Hegazi, “Removal of heavy metals from wastewater using agricultural and industrial wastes as adsorbents,” *HBRC Journal*, vol. 9, pp. 276-282, 2013.
- [4] M. Visa, “Synthesis and characterization of new zeolite materials obtained from fly ash obtained from fly ash,” *Powder Technology*, vol. 294, pp. 338-347, 2016.
- [5] M. Barakat, “New trends in removing heavy metals from industrial wastewater,” *Arabian Journal of Chemistry*, vol. 4, pp. 361-377, 2011.
- [6] M. Matouq, N. Jildeh, M. Qtaishat, M. Hindiyeh and M. Q. Al Syouf, “The adsorption kinetics and modeling for heavy metals removal from wastewater by Moringa pods,” *Journal of Environmental Chemical Engineering*, vol. 3, pp. 775-784, 2015.
- [7] M. S. Sankhla, M. Kumari, M. Nadan, R. Kumar and P. Agrawal, “Heavy Metals Contamination in Water and their Hazardous Effect on Human Health-A Review,” *International Journal of Current Microbiology and Applied Sciences*, vol. 5, no. 10, pp. 759-766, 2016.
- [8] M. Kumari, C. U. Pittman Jr. and D. Mohan, “Heavy metals [chromium (VI) and lead (II)] removal from water using mesoporous magnetite (Fe<sub>3</sub>O<sub>4</sub>) nanospheres,” *Journal of Colloid and Interface Science*, vol. 442, pp. 120-132, 2015.
- [9] S. K. Gunatilake, “Methods of Removing Heavy Metals from,” *Journal of Multidisciplinary Engineering Science Studies Industrial Wastewater*, vol. 1, no. 1, pp. 13-18, 2015.
- [10] Ihsanullah, A. Abbas, A. M. Al-Amer, T. Laoui, M. J. Al-Marri, Al-Marri, M. S. Nasser, M. Khraisheh and . M. Ali Atieh, “Heavy metal removal from aqueous solution by advanced carbon nanotubes: Critical review of adsorption applications,” *Separation and Purification Technology*, vol. 157, no. 8, pp. 141-161, 2016.
- [11] L. Changkun, B. Renbi and L. Quan San, “Selective removal of copper and lead ions by diethylenetriamine-functionalized adsorbent: Behaviors and mechanisms,” *Water Research*, vol. 42, no. 6-7, pp. 1511-1522, 2008.
- [12] J. Perić, M. Trgo and N. Vukohevic Medvidović, “Removal of zinc, copper and lead by natural zeolite—a comparison of adsorption isotherms,” *Water Research*, vol. 38, no. 7, pp. 1893-1899, 2004.

- [13] I. Mobasherpour, "Removal of divalent nickel cations from aqueous solution by multi-walled carbon nano tubes: equilibrium and kinetic processes," *Research on Chemical Intermediates*, vol. 38, no. 9, pp. 2205-2222, 2012.
- [14] E. Mazarío, A. S. Helal, J. Stemper, A. Mayoral, P. Decorse, A. Chevillor-Biraud, S. Novak, C. Perruchot, C. Lion, R. Losno, T. Le Gall, S. Ammar, J.-M. El Hage Chahine and M. Hémadi, "Maghemite nanoparticles bearing di(amidoxime) groups for the extraction of uranium from wastewaters," *AIP Advances*, vol. 7, no. 5, 2017.
- [15] W. Wei, W. Zhaohui, Y. Taekyung, J. Changzhong and K. Woo-Sik, "Recent progress on magnetic iron oxide nanoparticles: synthesis, surface functional strategies and biomedical applications," *Science and Technology of Advanced Materials*, vol. 16, no. 2, pp. 1-43, 2015.
- [16] W. Wu, Q. He and C. Jiang, "Magnetic Iron Oxide Nanoparticles: Synthesis and Surface Functionalization Strategies," *Nanoscale Research Letters*, vol. 3, pp. 397-415, 2008.
- [17] A. M. Gutierrez, T. D. Dziubla and J. Z. Hilt, "Recent Advances on Iron Oxide Magnetic Nanoparticles as Sorbents of Organic Pollutants in Water and Wastewater Treatment," *Reviews on Environmental Health*, vol. 32, pp. 111-117, 2017.
- [18] A. S. Teja and K. Pei-Yoong, "Synthesis, properties, and applications of magnetic iron oxide nanoparticles," *Progress in Crystal Growth and Characterization of Materials*, vol. 55, no. 1-2, pp. 22-45, 2009.
- [19] B. Vega, M. del Arco and C. Martín, "Magnetic Nanoparticles of Iron Oxide as Matrices from Controlled Release," *FarmaJournal*, vol. 1, no. 1, pp. 101-107, 2016.
- [20] P. Tartaj, M. P. Morales, S. Veintimillas-Verdaguer, T. González-Carreño and C. J. Serna, "The preparation of magnetic nanoparticles for applications in biomedicine," *Journal of Physics D: Applied Physics*, vol. 36, no. 13, pp. R182-R197, 2003.
- [21] L. Jae-Hyun, K. Ji-wook and C. Jinwoo, "Magnetic Nanoparticles for Multi-Imaging and Drug Delivery," *Molecules and Cells*, vol. 35, no. 4, pp. 274-284, 2013.
- [22] A. Figuerola, R. Di Corato, L. Manna and T. Pellegrino, "From iron oxide nanoparticles towards advanced iron-based inorganic materials designed for biomedical applications," *Pharmacological Research*, vol. 62, no. 2, pp. 126-143, 2010.
- [23] K. Hola, Z. Markova, G. Zoppellaro, J. Tucek and R. Zboril, "Tailored functionalization of iron oxide nanoparticles for MRI, drug delivery, magnetic separation and immobilization of biosubstances," *Biotechnology Advances*, vol. 33, no. 6, pp. 1162-1176, 2015.
- [24] Z. Wang, R. Qiao, N. Tang, Z. Lu, H. Wang, Z. Zhang, X. Xue, Z. Huang, Z. Siruo, G. Zhang and Y. Li, "Active targeting theranostic iron oxide nanoparticles for MRI and magnetic resonance-guided focused ultrasound ablation of lung cancer," *Biomaterials*, vol. 127, pp. 25-35, 2017.

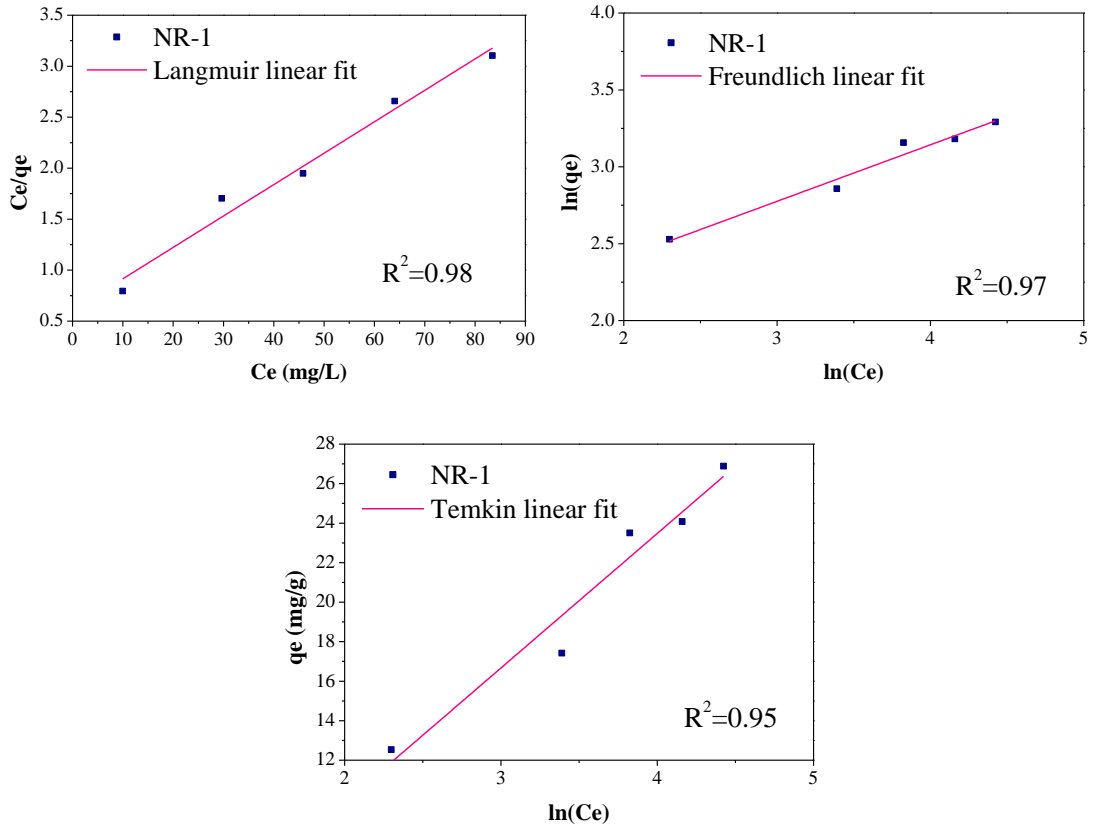
- [25] L. Nohyun, Y. Dongwon, L. Daishun, C. Mi Hyeon, H. Taeghwan and C. Jinwoo, "Iron Oxide Based Nanoparticles for Multimodal Imaging and Magnetoresponse Therapy," *Chemical Reviews*, vol. 115, no. 19, pp. 10637-10689, 2015.
- [26] G. Kandasamy, A. Sudame, T. Luthra, S. Kalawati and D. Maity, "Functionalized Hydrophilic Superparamagnetic Iron Oxide Nanoparticles for Magnetic Fluid Hyperthermia Application in Liver Cancer Treatment," *ACS Omega*, vol. 3, no. 4, pp. 3991-4005, 2018.
- [27] D. Feng, C. Aldrich and H. Tan, "Removal of heavy metal ions by carrier magnetic separation of adsorptive particulates," *Hydrometallurgy*, vol. 56, no. 3, pp. 359-368, 2000.
- [28] C. Zhi-Min, C. Zhe, C. Chang-Yan, J. Lei and S. Wei-Guo, "A yolk-shell structured Fe<sub>2</sub>O<sub>3</sub>@mesoporous SiO<sub>2</sub> nanoreactor for enhanced activity as a Fenton catalyst in total oxidation of dyes," *Chemical Communications*, vol. 49, no. 23, pp. 2332-2334, 2013.
- [29] K. L. Tan and B. H. Hameed, "Insight into the adsorption kinetics models for the removal of contaminants from aqueous solutions," *Journal of the Taiwan Institute of Chemical Engineers*, vol. 74, pp. 25-48, 2017.
- [30] Z. Zing, T. Xu, K. Su, H. Pengwei, S. Minshan, S. Weidong, L. Ziyang and Y. Yongsheng, "Constructing of the Magnetic Photocatalytic Nanoreactor MS@FCN for Cascade Catalytic Degrading of Tetracycline," *The Journal of Physical Chemistry C*, vol. 120, pp. 27250-27258, 2016.
- [31] Z. Ling, Q. Shizhang, J. Yonggang, C. Zhigan, G. Hongchen and Q. L. Gao, "Magnetic Hollow Spheres of Periodic Mesoporous Organosilica and Fe<sub>3</sub>O<sub>4</sub> Nanocrystals: Fabrication and Structure Control," *Advanced Materials*, vol. 20, pp. 805-809, 2008.
- [32] M. Kazemipour, M. Ansari, S. Tajrobehkar, M. Majdzadeh and H. R. Kermani, "Removal of lead, cadmium, zinc, and copper from industrial wastewater by carbon developed from walnut, hazelnut, almond, pistachio shell, and apricot stone," *Journal of Hazardous Materials*, vol. 150, pp. 322-327, 2008.
- [33] S. M. Ponder, J. G. Darab and T. E. Mallouk, "Remediation of Cr(VI) and Pb(II) Aqueous Solutions Using Supported, Nanoscale Zero-valent Iron," *Environmental Science and Technology*, vol. 34, no. 12, pp. 2564-2569, 2000.
- [34] C. Wang, X. Hu, M.-L. Chen and Y.-H. Wu, "Total concentrations and fractions of Cd, Cr, Pb, Cu, Ni and Zn in sewage sludge from municipal and industrial wastewater treatment plants," *Journal of Hazardous Materials*, vol. B119, pp. 245-249, 2005.
- [35] Y. Masaki, "Characteristics of Industrial Wastewater discharged from Industrialized Provinces and Specific Industrial Sectors in China based on the Official Statistical Reports," *Joint Journal of Novel Carbon Resource Sciences & Green Asia Strategy*, vol. 3, no. 2, pp. 59-67, 2016.
- [36] World Health Organization, "Lead in Drinking-water," 2011.

- [37] *Real Decreto 140/2003, de 7 de febrero, por el que se establecen los criterios sanitarios de la calidad del agua de consumo humano.*, 2003.
- [38] *Real Decreto 60/2011, de 21 de enero, sobre las normas de calidad ambiental en el ámbito de la política de aguas.*, 2011.
- [39] L. M. Bronstein, X. Huang, J. Retrum, A. Schmucker, M. Pink, B. D. Stein and B. Dragnea, "Influence of Iron Oleate Complex Structure on Iron Oxide Nanoparticle Formation," *Chemistry Materials*, vol. 19, no. 15, pp. 3624-3632, 2007.
- [40] C. Cannas, A. Musinu, A. Ardu, F. Orrù, D. Peddis, M. Casu, R. Sanna, F. Angius, G. Diaz and G. Piccaluga, "CoFe<sub>2</sub>O<sub>4</sub> and CoFe<sub>2</sub>O<sub>4</sub>/SiO<sub>2</sub> Core/Shell Nanoparticles: Magnetic and Spectroscopic Study," *Chemistry of Materials*, vol. 22, pp. 3353-3361, 2010.
- [41] A. Gallo-Cordova, M. d. M. Silva-Gordillo, G. A. Muñoz, X. Arboleda-Faini and D. Almeida Streitwieser, "Comparison of the adsorption capacity of organic compounds present in produced water with commercially obtained walnut shell and residual biomass," *Journal of Environmental Chemical Engineering*, vol. 5, no. 4, pp. 4041-4050, 2017.
- [42] M. Barbera and G. Gurnari, "Adsorption Equilibria," in *Wastewater Treatment and Reuse in the Food Industry*, Springer, 2018, pp. 35-36.
- [43] D. Robati, "Pseudo-second-order kinetic equations for modeling adsorption systems for removal of lead ions using multi-walled carbon nanotube," *Journal of Nanostructure in Chemistry*, vol. 55, no. 3, 2013.
- [44] L. Chen and J. Li, "A Study of  $\gamma$ -Fe<sub>2</sub>O<sub>3</sub> Nanoparticles Modified Using ZnCl<sub>2</sub> during Synthesis," *Advances in Materials Physics and Chemistry*, vol. 3, no. 1, pp. 31-35, 2013.
- [45] H. H. Imad, A. I. Israa and J. K. Hawraa, "Gas chromatography mass spectrum and fourier-transform infrared spectroscopy analysis of methanolic extract of Rosmarinus officinalis leaves," *Journal of Pharmacognosy and Phytotherapy*, vol. 7, no. 6, pp. 90-106, 2015.
- [46] Royal Society of Chemistry, "Infrared Spectroscopy (IR)," 2009.
- [47] P. J. Haines, "Chapter 1: Introduction to thermal methods," in *Thermal Methods of Analysis Principles, Applications and Problems*, Springer, 2012, pp. 1-20.
- [48] E. Vargas, M. Romero-Sáez, J. C. Denardin and F. Gracia, "The ultrasound-assisted synthesis of effective monodisperse nickel nanoparticles: magnetic characterization and its catalytic activity in CO<sub>2</sub> methanation," *New Journal of Chemistry*, vol. 40, pp. 7307-7310, 2016.
- [49] D. Ma, T. Veres, L. Clime, F. Normandin, J. Guan, D. Kingston and B. Simard, "Superparamagnetic Fe<sub>x</sub>O<sub>y</sub>@SiO<sub>2</sub> Core-Shell Nanostructures: Controlled Synthesis and Magnetic Characterization," *The Journal of Physical Chemistry C*, vol. 111, no. 5, pp. 1999-2007, 2007.

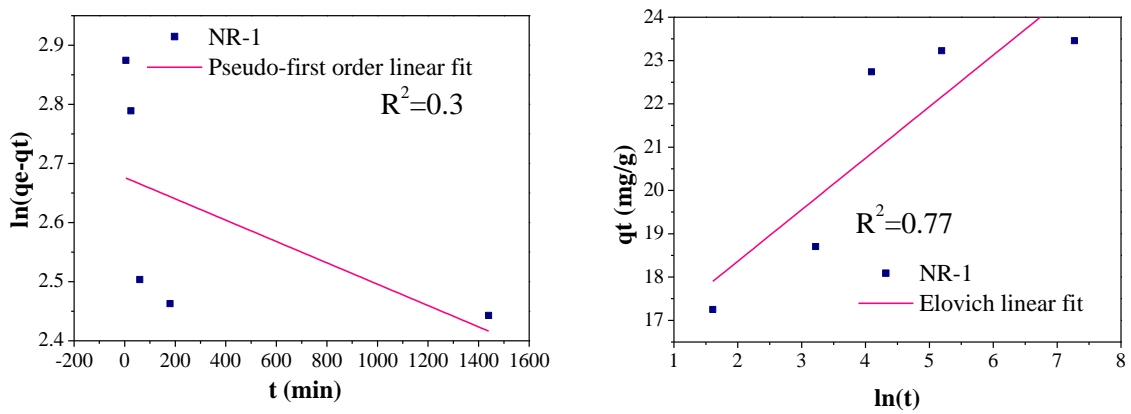
- [50] O. Arriortua, M. Insausti, L. Lezama, I. Gil de Muro, E. Garaio, J. Martínez de la Fuente, R. M. Fratila, M. P. Morales, R. Costa, M. Eceiza, M. Sagartzazu-Aizpurua and J. M. Aizpurua, "RGD-Functionalized Fe<sub>3</sub>O<sub>4</sub> nanoparticles for magnetic hyperthermia," *Colloids and Surfaces B: Biointerfaces*, vol. 165, pp. 315-324, 2017.
- [51] X. Lihui, W. Liming, S. Yong, Y. Ding and Z. Cai, "Preparation of Hexadecyltrimethoxysilane-modified Silica Nanocomposite Hydrosol and Superhydrophobic Cotton Coating," *Fibers and Polymers*, vol. 16, no. 5, pp. 1082-1091, 2015.
- [52] K. Y. Dong, L. Su Seong, G. C. Papaefthymiou and J. Y. Ying, "Nanoparticle Architectures Templated by SiO<sub>2</sub>/Fe<sub>2</sub>O<sub>3</sub> Nanocomposites," *Chemistry of Materials*, vol. 18, no. 3, pp. 614-619, 2006.
- [53] S. Brunauer, P. H. Emmet and E. Teller, "Adsorption of Gases in Multimolecular Layers," *Journal of the American Chemical Society*, vol. 60, no. 2, pp. 309-319, 1938.
- [54] J. U. Keller and R. Staudt, "Chapter 7: Adsorption Isotherms," in *Gas Adsorption Equilibria*, Springer, 2005, pp. 359-413.
- [55] D. Shengxia, T. Rongfeng, X. Zechun, Z. Xianxi, Z. Yueying, Z. Wen, Z. Junhong, W. Bingquan, Z. Suyuan and S. Dezhi, "Effective removal of Pb(II) using magnetic Co<sub>0.6</sub>Fe<sub>2.4</sub>O<sub>4</sub> micro-particles as the adsorbent: Synthesis and study on the kinetic and thermodynamic behaviors for its adsorption," *Colloids and Surfaces A: Physicochemical and Engineering Aspects*, vol. 469, no. 20, pp. 211-223, 2015.
- [56] P. Xu, G. M. Zeng, D. L. Huang, C. Lai, M. H. Zhao, Z. Wei, N. Jie Li, C. Huan and G. Xin Xie, "Adsorption of Pb(II) by iron oxide nanoparticles immobilized Phanerochaete chrysosporium: Equilibrium, kinetic, thermodynamic and mechanisms analysis," *Chemical Engineering Journal*, vol. 203, pp. 423-431, 2012.
- [57] M. Hua, S. Zhang, B. Pan, W. Zhang, L. Lv and Q. Zhang, "Heavy metal removal from water/wastewater by nanosized metal oxides: A review," *Journal of Hazardous Materials*, Vols. 211-212, pp. 3170-331, 2012.
- [58] K. E. Engates and H. J. Shipley, "Adsorption of Pb, Cd, Cu, Zn, and Ni to titanium dioxide nanoparticles: effect of particle size, solid concentration, and exhaustion," *Environmental Science and Pollution Research*, vol. 18, no. 3, pp. 386-395, 2011.
- [59] J.-R. Li, R. J. Kuppler and H.-C. Zhou, "Selective gas adsorption and separation in metal-organic frameworks," *Chemical Society Reviews*, vol. 98, pp. 1477-1504, 2009.
- [60] N. N. Nassar, "Rapid removal and recovery of Pb(II) from wastewater by magnetic nanoadsorbents," *Journal of Hazardous Materials*, vol. 184, pp. 538-546, 2010.
- [61] M. Horsfall and A. I. Spiff, "Effects of temperature on the sorption of Pb<sup>2+</sup> and Cd<sup>2+</sup> from aqueous solution by Caladium bicolor (Wild Cocoyam) biomass," *Electronic Journal of Biotechnology*, vol. 8, no. 2, pp. 162-169, 2005.

## 8. Annexes

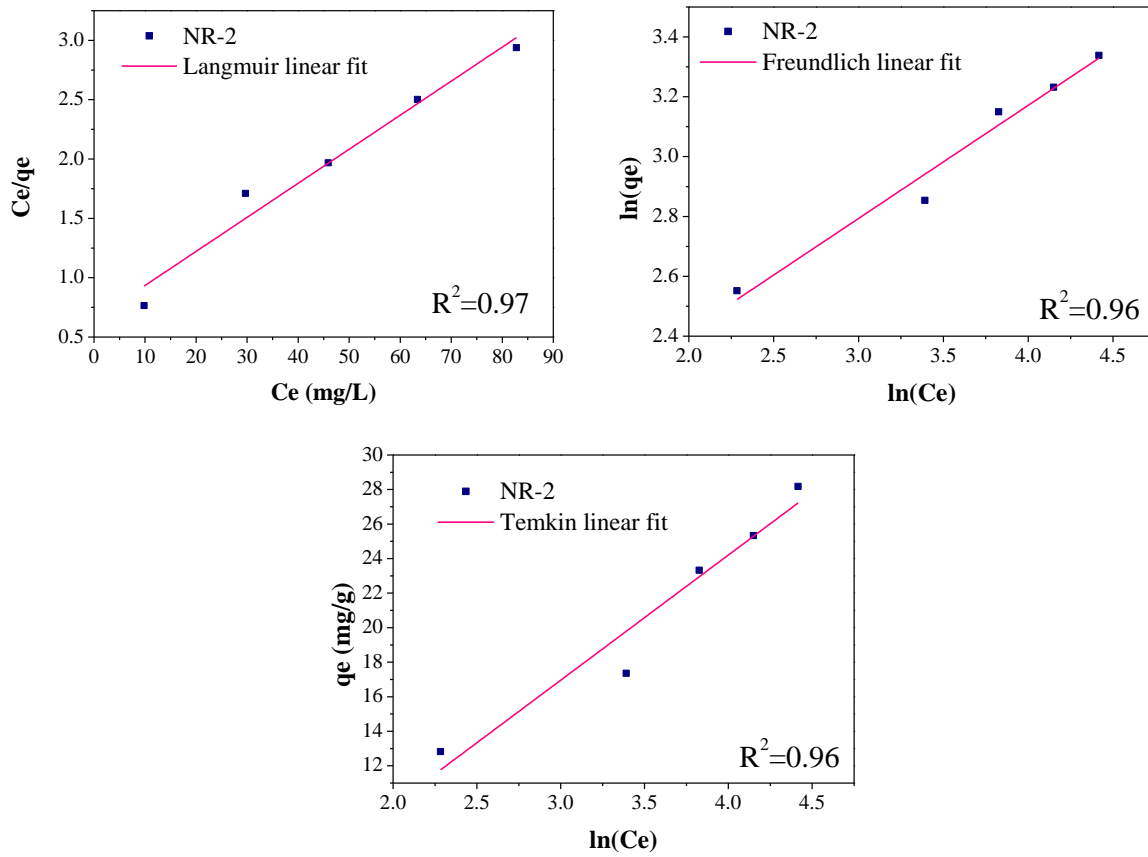
**Annex 1** Linear isotherms of NR-1 adsorption data



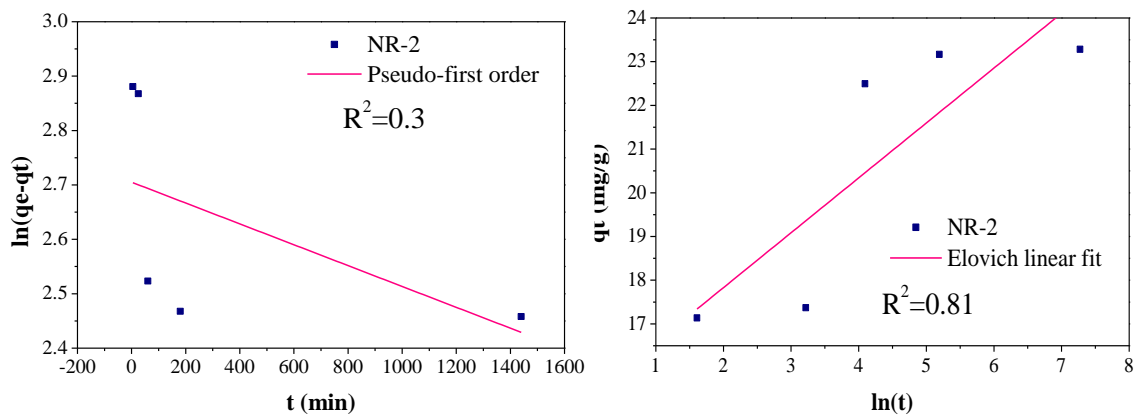
**Annex 2** Linear kinetic models of NR-1 adsorption data



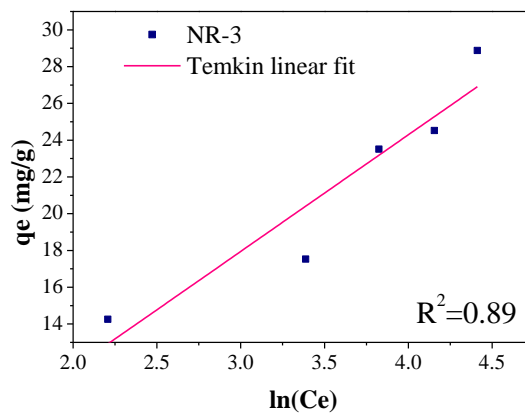
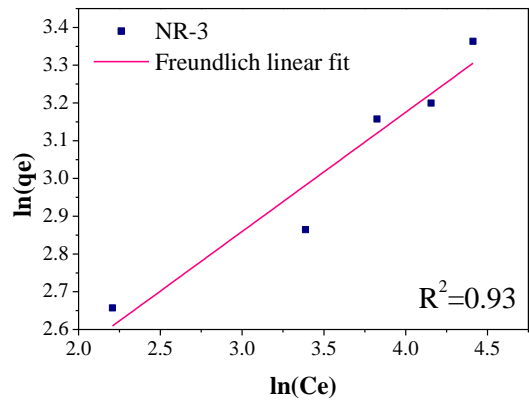
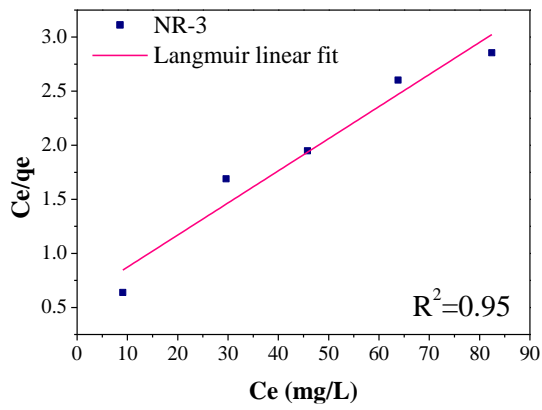
### Annex 3 Linear isotherms of NR-2 adsorption data



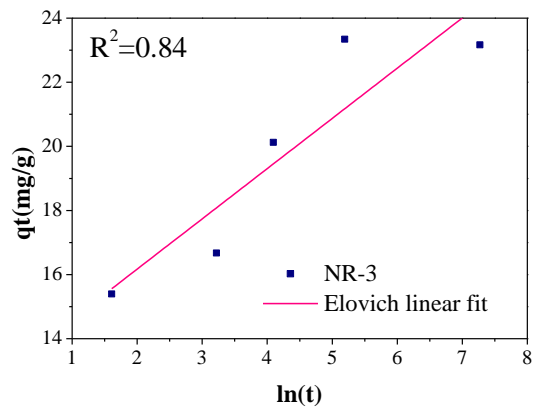
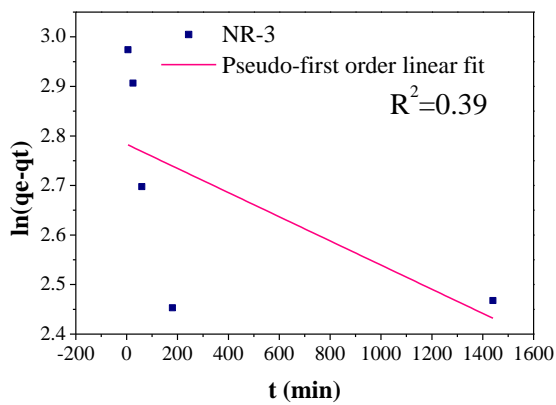
### Annex 4 Linear kinetic models of NR-2 adsorption data



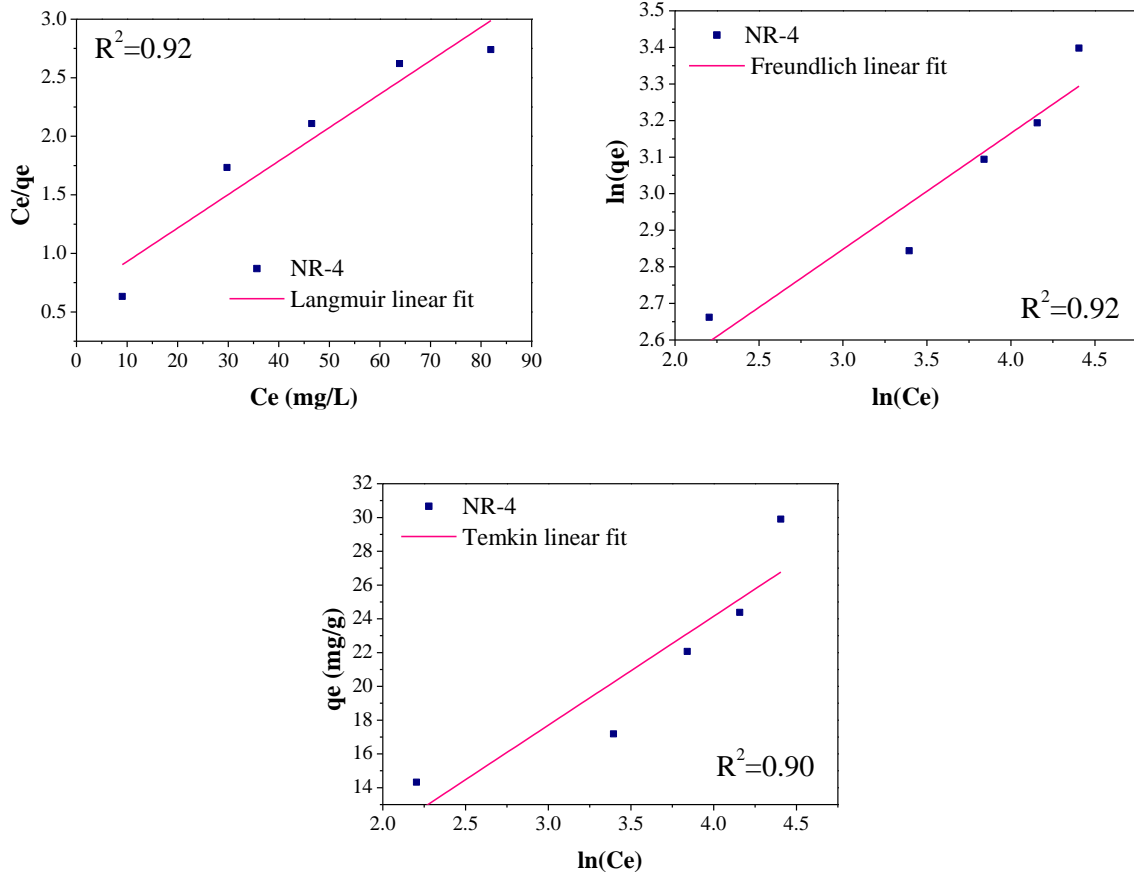
**Annex 5** Linear isotherms of NR-3 adsorption data



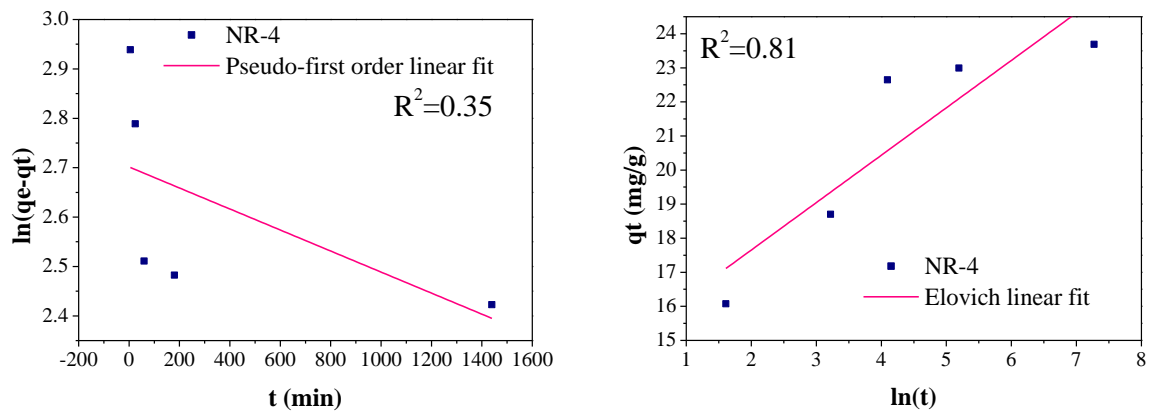
**Annex 6** Linear kinetic models of NR-3 adsorption data



### Annex 7 Linear isotherms of NR-4 adsorption data



### Annex 8 Linear kinetic models of NR-4 adsorption data



**Annex 9** Constants for the theoretic calculation of Pb<sup>2+</sup> removal using nanoreactors

Parameter	Acronim	Value	Unit
NR mass	NRm	0.005	g
Volume (V)	V	0.01	L
Pb size	Pb <sub>size (radius)</sub>	2.02E-10	m
Pb weight	MW <sub>Pb</sub>	207.2	g/mol
Core radius	r <sub>core</sub>	6.00E-09	m
NR radius	r <sub>NR</sub>	2.50E-08	m
ρ <sub>magnetite</sub>	ρ <sub>core</sub>	5.20E+06	g/m <sup>3</sup>
ρ <sub>silica</sub>	ρ <sub>silica</sub>	2.65E+06	g/m <sup>3</sup>
Avogadro	NA	6.02E+23	atoms/mol

**Annex 10** Variables and equations for theoretic calculation of Pb<sup>2+</sup> removal using nanoreactors

Parameter	Acronim	Equation	Unit
Internal surface	S <sub>in</sub>	A <sub>BET</sub> * NRmass	m <sup>2</sup>
Experimental lead removal	[Pb] <sub>Removed</sub>	[Pb] <sub>0</sub> - [Pb] <sub>f</sub>	mgPb/L
Experimental lead mass removed	m <sub>exp</sub>	[Pb] <sub>Removed</sub> * V	mg Pb
Lead surface	S <sub>Pb</sub>	π*r <sup>2</sup>	m <sup>2</sup>
Nanoreactor surface	S <sub>NR</sub>	4*π*r <sup>2</sup>	m <sup>2</sup>
Magnetite core volume	V <sub>Core</sub>	(4/3)*π*r <sub>core</sub> <sup>3</sup>	m <sup>3</sup>
Silica and silica porogenic-shell volume	V <sub>silica</sub>	((4/3)*π*r <sub>NR</sub> <sup>3</sup> )-V <sub>core</sub>	m <sup>3</sup>
Magnetite core mass	m <sub>Core</sub>	ρ <sub>core</sub> * V <sub>core</sub>	g
Silica-shell mass	m <sub>silica</sub>	ρ <sub>silica</sub> * V <sub>silica</sub>	g
Nanoreactor total mass	m <sub>NR</sub>	m <sub>core</sub> + m <sub>silica</sub>	g
External surface area	B	S <sub>NR</sub> /m <sub>NR</sub>	m <sup>2</sup> /g
External surface	S <sub>EXT</sub>	B * NRm	m <sup>2</sup>
Theoretic external lead mass removed	m <sub>exteoric</sub>	(S <sub>EXT</sub> * MW <sub>Pb</sub> )/(S <sub>Pb</sub> * NA)	mg/Pb

**Annex 11** Experimental data of Pb<sup>2+</sup> removal using nanoreactors

Sample	A <sub>BET</sub> (m <sup>2</sup> /g)	q <sub>max</sub> mg/gNR	S <sub>total</sub> m <sup>2</sup>	S <sub>external</sub> m <sup>2</sup>	S <sub>internal</sub> m <sup>2</sup>	[Pb] <sub>0</sub> (mg Pb/L)	[Pb] <sub>f</sub> (mg Pb/L)	[Pb] <sub>Removed</sub> (mg Pb/L)	m <sub>exp</sub> (mgPb)
NR-1	470	34.483	2.35	0.223	2.127	96.88	83.439	13.441	0.134
NR-2	522	34.130	2.61	0.223	2.387	96.88	82.793	14.087	0.141
NR-3	478	33.223	2.39	0.223	2.167	96.88	82.441	14.439	0.144
NR-4	568	34.483	2.84	0.223	2.617	96.88	81.928	14.952	0.150

**Annex 12** Theoric calculation of Pb<sup>2+</sup> removal using nanoreactors

<b>Parameter</b>	<b>Acronim</b>	<b>Value</b>	<b>Unit</b>
Lead surface	S <sub>Pb</sub>	1.2819E-19	m <sup>2</sup>
Nanoreactor surface	S <sub>NR</sub>	7.85E-15	m <sup>2</sup>
Magnetite core volume	V <sub>Core</sub>	9.05E-25	m <sup>3</sup>
Silica and silica porogenic-shell volume	V <sub>silica</sub>	6.45E-23	m <sup>3</sup>
Magnetite core mass	m <sub>Core</sub>	4.70E-18	g
Silica-shell mass	m <sub>silica</sub>	1.71E-16	g
Nanoreactor total mass	m <sub>NR</sub>	1.76E-16	g
External surface area	B	44.69	m <sup>2</sup> /g
External surface	S <sub>EXT</sub>	0.223	m <sup>2</sup>
Theoric external lead mass removed	m <sub>exteoric</sub>	0.600	mg Pb

<b>Sample</b>	<b>Diameter TEM size (m)</b>	<b>m<sup>theoric</sup> external (mgPb)</b>	<b>m<sup>theoric</sup> internal (mgPb)</b>	<b>m<sup>theoric</sup> total (mgPb)</b>	<b>Theoric q<sub>max</sub> (mg Pb/g)</b>	<b>External occupancy %</b>	<b>Total occupancy %</b>
NR-1	5.00E-08	0.600	5.71	6.308	1262	22.4	2.1
NR-2	5.00E-08	0.600	6.41	7.005	1401	23.5	2.0
NR-3	5.00E-08	0.600	5.82	6.415	1283	24.1	2.3
NR-4	5.00E-08	0.600	7.02	7.623	1525	24.9	2.0